1

# Transient Stability and Active Protection of Power Systems with Grid-Forming PV Power Plants

Soummya Roy, Student Member, IEEE and Hugo N. Villegas Pico, Member, IEEE

Abstract—Photovoltaic (PV) power plants with grid-forming technology must withstand severe disturbances and remain operational. To address this challenge, this paper sets-forth a grid-forming strategy for PV solar power plants so that they can ride through power system faults. This capability is accomplished by leveraging two-axis proportional-integral regulators with anti-windup functionality. This paper also demonstrates that fluctuations of solar irradiance can cause significant dc-link voltage variations and loss of synchronism of grid-forming PV plants. Hence, we develop an active dc-link protection method which depends on estimation of solar irradiance. The contributions of this paper are demonstrated via positive-sequence simulations of modified versions of the WSCC 9- and IEEE 39-bus grids.

Index Terms-Photovoltaic systems, power system protection.

## I. Introduction

THE transient stability of power systems with massive penetration of grid-forming power converters is challenging to ascertain. In particular, this task is difficult to address because grid-forming strategies that are reliable to faults are still under research [1]–[3]. Studying the dynamic performance of converter-based assets with grid-forming technology during large disturbances is timely to identify problems and engineer solutions. Notably, the advancement of grid-forming technology is of national interest in the United States of America [4].

Grid-forming controls are attractive because converters powered by non-conventional energy resources, e.g., wind and solar, could autonomously self-energize or black start [5]. Hence, power grids with ultra-high penetrations of converter-based generation can be possible. This contrasts present control technology for power converters that resort to phase-locked loops which depend on externally generated voltages, e.g, by synchronous machines [6], [7]. Proposed grid-forming techniques use speed-droop, virtual synchronous machine, and virtual oscillator algorithms [7]–[19], to name a few.

In recent years, photovoltaic (PV) power plants in the U.S. have faced several transient events. For instance: (i) The 2021 Odessa disturbance, by a fault in a transformer, caused the disconnection of 1,112 MW of PV power [20]. (ii) The 2020 San Fernando disturbance led to the reduction of more than 1,000 MW of PV production [21]. (iii) The 2018 Palmdale Roost and Angeles Forest event caused the reduction of more than 1,000 MW of PV power [22]. (iv) The 2017 Canyon 2 Fire disturbance caused the disconnection of 900 MW of

This material is based upon work supported by the National Science Foundation under Grant No. 2013739.

S. Roy and H. N. Villegas Pico are with Iowa State University, Ames, IA 50011, USA (e-mail: {soummyar, hvillega}@iastate.edu).

PV power [23]. (v) The 2016 Blue Cut Fire event caused the disconnection of 1,200 MW of PV power [24]. In the future, similar events might repeat and challenge emerging grid-forming technologies. Further, these issues might also extrapolate worldwide because PV capacity is reaching Terawatt levels [25]. To the Authors' knowledge, there are no utility-scale grid-forming PV power plants deployed in the U.S.; nonetheless, they are likely to be ubiquitous in the future [4].

A widely adopted assumption in the design and testing phases of grid-forming technology is that the dc-link voltage of power converters does not vary in time [7]–[19]. However, PV power might suddenly drop if solar irradiance reduces which can lead to dc-link voltage regulation problems. Even if converters are powered by both PV arrays and batteries, there could be instances when batteries fully discharge during sunlight times. If there is no sunlight and batteries are discharged, power operators must resort to wind turbines, for example, for energy adequacy [26]. Another problem pertains to incorporating the models of grid-forming assets into positive-sequence simulations. Typically, a center of inertia is defined to model relative rotor angles of synchronous machinery [27]–[29]. However, this definition does not apply to power systems with speed-droop grid-forming converters.

To address the aforementioned problems, this paper reports the following advances: (i) A positive-sequence model of a grid-forming PV-solar power plant that is capable of riding through faults. In particular, we innovate the voltage control strategy for current-regulated PWM converters in [30] by incorporating two-axis anti-windup PI regulators. The novelty is that we extend the one-axis anti-windup series implementation of [31, p. 91] to two-axis systems which control inputs are bounded by a circle. (ii) A definition of a hypothetical center of inertia to model in the positive-sequence domain grids with a mix of machines and converters as well as power converters only. In particular, the proposed definition enables the possibility of simulating power systems with power converters steered only by droop controls in a positive-sequence domain. (iii) A condition in which PV power plants can lose synchronism. We showcase that grid-forming PV power plants can lose synchronism during variations of solar irradiance as impacting dc-link voltage. (iv) An active protection strategy to prevent dc-link voltage fluctuations during solar irradiation disturbances. To that end, we engineer a method to estimate solar irradiance using: an abstract PV array model, PV current, and dc-link voltage. The protection interfaces with the classical droop-control law [8]. This paper is significant for the reliable integration of grid-forming PV power plants into power grids and to ascertain compliance with grid codes [32], [33].

The rest of the paper is organized as follows. Section II frames a general model of a power system with conventional and grid-forming PV power plants. Section III establishes a model of PV plants with fault ride-though capability and theory for stable grid-forming operation. Section IV engineers an active dc-link protection against solar irradiance variations. Section V consolidates a multi-machine multi-converter power system in the positive-sequence domain. In Section VI, we leverage illustrative case studies to highlight the contributions of this paper. Section VII concludes our exposition.

# II. Preliminaries

A power system with conventional and PV solar power plants is modeled with a set of differential-algebraic equations:

$$\frac{d}{dt}\mathbf{x} = \mathcal{F}(\mathbf{x}, \mathbf{y}, \mathbf{u}, \mathbf{w}) \tag{1}$$

$$\mathbf{0} = \mathscr{G}_{\gamma}(\boldsymbol{x}, \boldsymbol{y}, \boldsymbol{u}, \boldsymbol{w}) \tag{2}$$

$$\Psi = \mathscr{H}(x, y, u, w) \tag{3}$$

for  $t \in [0, T]$ ,  $\gamma \in \{1, 2, 3\}$ , and  $\boldsymbol{x}(0) = \boldsymbol{x}_0$ . Here,  $\mathscr{F} : \mathbb{R}^{n_x} \times$  $\mathbb{R}^{n_y} \times \mathbb{R}^{n_u} \times \mathbb{R}^{n_w} \mapsto \mathbb{R}^{n_x}, \mathscr{G}_{\gamma} : \mathbb{R}^{n_x} \times \mathbb{R}^{n_y} \times \mathbb{R}^{n_u} \times \mathbb{R}^{n_w} \mapsto \mathbb{R}^{n_y}$ and  $\mathscr{H}: \mathbb{R}^{n_x} \times \mathbb{R}^{n_y} \times \mathbb{R}^{n_u} \times \mathbb{R}^{n_w} \mapsto \mathbb{R}^{n_\Psi}$ . The parameter T is the simulation time. The vector  $\boldsymbol{x} \in \mathbb{R}^{n_x}$  encapsulates state information of I synchronous machines, J PV plants, and K motor loads. The vector  $\boldsymbol{y} \in \mathbb{R}^{n_y}$  models algebraic variables that arise in the transmission system. The vector  $oldsymbol{u} \in \mathbb{R}^{n_u}$  models a set of commands that are used to drive the grid to a desirable state. The vector  $w \in \mathbb{R}^{n_w}$  models exogenous disturbances to the system, e.g., variability of solar irradiation. The vector  $\mathbf{\Psi} \in \mathbb{R}^{n_{\Psi}}$  models observations, such as voltage and current magnitudes, at particular points in the grid. The parameter  $\gamma$  indexes the transmission system topologies before  $\gamma = 1$ , during  $\gamma = 2$ , and after a fault  $\gamma = 3$ . All variables and parameters are per-unit quantities with respect to a common volt-ampere base  $S_b$  and a speed base  $\omega_b$ .

## A. Transformation of Variables

We consider positive-sequence abc waveforms of the form:

$$f_{abc} = F \left[ \cos(\theta_f), \cos(\theta_f - \frac{2\pi}{3}), \cos(\theta_f + \frac{2\pi}{3}) \right]^{\top}$$
 (4)

where f represents either voltages or currents. Note here Fmodels per-unit rms magnitude. The angle  $\theta_f$  cycles at a synchronous speed. As commonly done in positive-sequence analysis, abc waveforms observed at a various points of a power grid are abstracted into dq-axis variables via [34]:

$$[f_d^{\nu}, f_q^{\nu}]^{\top} = \frac{2}{3} T(\theta_{\nu}) [f_a, f_b, f_c]^{\top}$$
 (5)

$$[f_d^{\nu}, f_q^{\nu}]^{\top} = \frac{2}{3} T(\theta_{\nu}) [f_a, f_b, f_c]^{\top}$$

$$T(\theta_{\nu}) = \begin{bmatrix} \cos(\theta_{\nu}) & \cos(\theta_{\nu} - 2\pi/3) & \cos(\theta_{\nu} + 2\pi/3) \\ -\sin(\theta_{\nu}) & -\sin(\theta_{\nu} - 2\pi/3) & -\sin(\theta_{\nu} + 2\pi/3) \end{bmatrix}$$
(5)

Here,  $\theta_{\nu}$  models the angle of a  $\nu$  reference frame satisfying:

$$\frac{d}{dt}\theta_{\nu} = \omega_b \omega_{\nu} \tag{7}$$

with  $\omega_{\nu}$  per-unit angular speed in the  $\omega_b$  base.

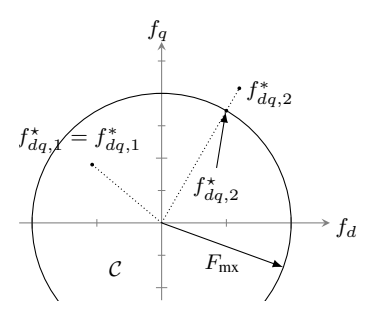


Fig. 1. Representation of a dq saturation function  $\mathcal{S}$ . A full circle is not shown to economize space.

#### B. Notation and Nomenclature

To abbreviate notation throughout the paper, we define:

$$f_{da}^{\nu} \triangleq [f_d^{\nu}, f_a^{\nu}]^{\top} \text{ and } f_{ad}^{\nu} \triangleq [f_a^{\nu}, -f_d^{\nu}]^{\top}.$$
 (8)

The superscript  $\nu \in \{e, r_1, \dots, r_i, \dots, r_I, c_1, \dots, c_j, \dots, c_J\}$ serves to the indicate either the synchronous e, i-th rotor  $r_i$ , and j-th converter  $c_j$  reference frames that are used in (5). We use J + I + 1 reference frames in this paper. The speeds of the reference frames are in (14), (34), and (37).

The naming convention of variables and parameters is introduced here by example. In the j-th PV power plant of Fig. 2 in Section III,  $i_{dq,f}^{c_j} = [i_{d,f}^{c_j}, i_{q,f}^{c_j}]^{\top}$  [which arise from (5)] are used to denote dq filter currents in the  $c_j$ reference frame. The parameters  $X_{f,j}$  and  $r_{f,j}$  of Fig. 2 denote filter reactance and filter resistance of the j-th PV plant. Please, note here that superscripts identify reference frames and subscripts differentiate parameters. This convention also applies to synchronous machines in Section II-D.

## C. Special Transformations and Functions

In this paper, variables in the ' $r_i$ ' or ' $c_i$ ' frames are actively mapped into the 'e' one and vice-versa with [34]:

$$\widetilde{F} = f_d^{\mathsf{e}} + \mathsf{j} f_q^{\mathsf{e}} = (f_d^{\mu} + \mathsf{j} f_q^{\mu}) e^{\mathsf{j} \delta_{\mu}}. \tag{9}$$

where  $\delta_{\mu}=\theta_{\mu}-\theta_{\rm e},\ \mu\in\{{\rm r}_i\,,{\rm c}_j\}$  for any i and j.  $\widetilde{F}$  is a phasor form of  $F\cos(\theta_f)$  in (4).

We employ  $\mathcal{M}: \mathbb{R}^2 \to \mathbb{R}$  and  $\mathcal{S}: \mathbb{R}^2 \times \mathbb{P} \to \mathbb{R}^2$  such that:

$$\mathscr{M}(f_{dq}^{\nu}) = \sqrt{(f_d^{\nu})^2 + (f_q^{\nu})^2} \tag{10}$$

$$\mathscr{S}(f_{dq}^{\nu}; F_{\text{mx}}) = \begin{cases} f_{dq}^{\nu} & \text{if } F \leq F_{\text{mx}} \\ f_{dq}^{\nu} \frac{F_{\text{mx}}}{F} & \text{if } F > F_{\text{mx}} \end{cases}$$
(11)

with  $F = \mathcal{M}(f_{dq}^{\nu})$  to simplify exposition. The function  $\mathscr{S}(\cdot; F_{\text{mx}})$  is critical to saturate current and voltage commands during faults without impacting control directionality. The behavior of  $\mathscr S$  in (11) is illustrated in Fig. 1. There,  $f_{dq,1}^*=f_{dq,1}^*$  because  $f_{dq,1}^*$  belongs to the origin-centered circle  $\mathscr C$  of radius  $F_{\rm mx}$ . On the other, hand  $f_{dq,2}^*=\mathscr S(f_{dq,2}^*,F_{\rm mx})$  is at the intersection of the boundary of  $\mathscr C$  and the line joining the center of C with  $f_{dq,2}^*$  because  $f_{dq,2}^*$  does not belong to C.

## D. Conventional Power Plants

The IEEE 1.1 model of an *i*-th (i = 1, ..., I) synchronous machine in the 'r<sub>i</sub>' reference frame is [29]:<sup>1</sup>

$$\frac{d}{dt}e_d^{r_i} = -\frac{1}{\tau_{do,i}} \left( e_d^{r_i} - (X_{d,i} - X'_{d,i})i_q^{r_i} - e_{fd,i} \right)$$
(12)

$$\frac{d}{dt}e_{q}^{\mathbf{r}_{i}} = -\frac{1}{\tau_{qq,i}} \left( e_{q}^{\mathbf{r}_{i}} + (X_{q,i} - X'_{q,i})i_{d}^{\mathbf{r}_{i}} \right) \tag{13}$$

$$\frac{d}{dt}\omega_{\mathbf{r}_i} = \frac{1}{2H_{\mathbf{r}_i}}(T_{m,i} - T_{e,i}) \text{ with } T_{e,i} = e_d^{\mathbf{r}_i}i_d^{\mathbf{r}_i} + e_q^{\mathbf{r}_i}i_q^{\mathbf{r}_i} \quad (14)$$

$$\frac{d}{dt}\delta_{\mathbf{r}_i} = \omega_b(\omega_{\mathbf{r}_i} - \omega_{\mathbf{e}}). \tag{15}$$

The variables  $e_d^{r_i}$ ,  $e_q^{r_i}$  model d- and q-axis voltages behind a transient impedance  $r_s + \mathrm{j} X'_{d,i}$  whereas  $i_d^{r_i}$ ,  $i_q^{r_i}$  are currents injected into a transmission network. The parameters  $\tau_{do,i}$ ,  $\tau_{qo,i}$ ,  $X_{d,i}$ ,  $X'_{d,i}$ ,  $X_{q,i}$ ,  $X'_{q,i}$ , and  $H_{r_i}$  are explained in [29, p. 32]. The form of relative rotor angle dynamics in (15) is because rotor speed  $\omega_{r_i}$  and  $\omega_{\mathrm{e}}$  are in per unit. The prime mover torque is  $T_{m,i}$  and the exciter field voltage is  $e_{fd,i}$ .

The torque dynamics by an *i*-th prime mover is:

$$\frac{d}{dt}T_{m,i} = \begin{cases}
-\frac{1}{\tau_{ch,i}}(T_{m,i} - P_{v,i}) & \text{if thermal} \\
-\frac{2}{\tau_{w,i}}(T_{m,i} - P_{v,i} + \tau_{w,i}\frac{d}{dt}P_{v,i}) & \text{if hydro}.
\end{cases}$$
(16)

Speed control is via a governor with speed droop  $R_{d,i}$  [29]:

$$\frac{d}{dt}P_{v,i} = -\frac{1}{\tau_{v,i}} \left( P_{v,i} - P_{v,i}^{\star} + P_{\omega,i} \right), \ P_{\omega,i} = \frac{\omega_{r_i} - 1}{R_{d,i}}.$$
(17)

The parameter  $\tau_{ch,i}$  is the steam chest time constant,  $\tau_{w,i}$  is the water time constant, and  $\tau_{v,i}$  is the valve time constant. The valve position command  $P_{v,i}^{\star}$  is from an operator. The units of  $T_{m,i}$  and  $P_{v,i}$  in (16) are equal in per unit.

The *i*-th exciter, stabilizer and amplifier dynamics are [29]:

$$\frac{d}{dt}e_{fd,i} = -\frac{1}{\tau_{e,i}} \left( (k_{e,i} + S_e^i(e_{fd,i})) e_{fd,i} - v_{a,i} \right)$$
 (18)

$$S_e^i(e_{fd,i}) = A_i e^{B_i e_{fd,i}}$$
(19)

$$\frac{d}{dt}r_{f,i} = -\frac{1}{\tau_{f,i}} \left( r_{f,i} - \frac{k_{f,i}}{\tau_{f,i}} e_{fd,i} \right)$$
 (20)

$$\frac{d}{dt}v_{a,i} = -\frac{1}{\tau_{a,i}}(v_{a,i} - k_{a,i}v_{e,i})$$
 (21)

$$-v_{a,\mathsf{mx},i} \le v_{a,i} \le v_{a,\mathsf{mx},i} \,. \tag{22}$$

For parameter explanation, please, refer to [29, p. 56-69]. The control error in (21) is:

$$v_{e,i} = V_i^* - V_i + r_{f,i} - \frac{k_{f,i}}{\tau_{f,i}} e_{fd,i}.$$
 (23)

The terminal voltage of an *i*-th machine is:

$$V_i = \mathcal{M}(v_{dq}^{r_i}) \text{ with } v_{dq}^{r_i} = e_{dq}^{r_i} - r_{s,i} i_{dq}^{r_i} + X'_{d,i} i_{qd}^{r_i}.$$
 (24)

<sup>1</sup>The IEEE 1.1 model is considered here to simplify exposition on electric machinery. The IEEE 2.2 representation can be readily used [29, p. 80]

## III. GRID-FORMING PV POWER PLANT

We illustrate in Fig. 2 a j-th  $(j \in \{1, \dots, J\})$  aggregated representation of several utility-scale grid-forming PV power inverters that constitute a PV power plant. The representation is obtained by using the structure-preserving technique reported in [6], [35]. It employs the fact that the current observed at the terminals of the aggregated model must be equal to the summation of the current output by individual inverters. It also considers that the topology, controls, and set-points of all PV inverters are identical which is a judicious assumption for PV power plants. In Fig. 2, the grid-side converter (GSC) is powered by a PV array and steered by a grid-forming regulator. The PV power plant is interconnected to a bulk power system via an ac inductive-capacitive-inductive (LCL) filter and a step-up transformer which is not shown.

The inputs to the grid-forming regulator are: (i) ac voltage magnitude  $V_j^{\star}$  and active power  $P_{e,j}^{\star}$  dispatch commands from a grid operator, (ii) dq-axis GSC currents  $i_{dq,f}^{\mathsf{c}_j}$ , (iii) dq-axis grid-side currents  $i_{dq,g}^{\mathsf{c}_j}$ , (iv) dq-axis voltages  $v_{dq,o}^{\mathsf{c}_j}$  at the ac capacitor node, as well as (v) dc-link voltage  $v_{dq,g}$  and PV-array current  $i_{pv,j}$ . The variables  $i_{dq,f}^{\mathsf{c}_j}$ ,  $i_{dq,g}^{\mathsf{c}_j}$ ,  $v_{dq,o}^{\mathsf{c}_j}$  arise by mapping abc quantities into a  $\mathsf{c}_j$  reference frame, q.v. (5). The signals  $v_{dc,j}$  and  $i_{pv,j}$  are used to estimate solar irradiance,  $I_{r,j}$ , observed by the PV array. This serves also to protect  $v_{dc,j}$  from reaching low values during irradiance drops.

## A. Ac- and Dc-Side Dynamics

We model the passive elements in Fig. 2. The dynamics of a *j*-th LCL filter (j = 1, ..., J) in the  $c_i$  frame are [36]:

$$\frac{d}{dt}i_{dq,f}^{c_j} = \frac{\omega_b}{X_{f,j}}(-r_{f,j}i_{dq,f}^{c_j} + \omega_{c_j}X_{f,j}i_{qd,f}^{c_j} + v_{dq,f}^{c_j} - v_{dq,o}^{c_j})$$
(25)

$$\frac{d}{dt}v_{dq,c}^{\mathbf{c}_j} = \frac{\omega_b}{B_{c,j}}(\omega_{\mathbf{c}_j}B_{c,j}v_{qd,c}^{\mathbf{c}_j} + i_{dq,f}^{\mathbf{c}_j} - i_{dq,g}^{\mathbf{c}_j})$$
(26)

$$v_{dq,o}^{c_j} = v_{dq,c}^{c_j} + r_{c,j} (i_{dq,f}^{c_j} - i_{dq,g}^{c_j}).$$
 (27)

The energy stored by the dc capacitor,  $E_{dc,j} = v_{dc,j}^2$ , meets:

$$\frac{d}{dt}E_{dc,j} = \frac{1}{B_{C,j}}(P_{pv,j} - P_{cv,j})$$
 (28)

with  $P_{pv,j}$  and  $P_{cv,j}$  the power sourced and withdrawn by the PV array and the GSC, respectively. The parameter  $B_{C,j}$  is the ratio between the capacitor energy at rated dc voltage and a common MVA base  $S_b$ . In Fig. 2,

$$P_{cv,j} = v_{d,f}^{c_j} i_{d,f}^{c_j} + v_{q,f}^{c_j} i_{q,f}^{c_j}$$
 (29)

appears in the dc and ac sides of the GSC, considered lossless. A low  $v_{dc,j}$  event can occur if  $I_{r,j}$  drops because this can lead to  $P_{pv,j} < P_{cv,j}$  which means that  $dE_{dc,j}/dt < 0$  in (28).

For control purposes, we consider  $P_{e,j}$  and  $Q_{e,j}$  [8]:

$$\frac{d}{dt}\widetilde{P}_{e,j} = \frac{1}{\tau_{s,i}}(-\widetilde{P}_{e,j} + P_{e,j}) \tag{30}$$

$$\frac{d}{dt}\widetilde{Q}_{e,j} = \frac{1}{\tau_{s,j}}(-\widetilde{Q}_{e,j} + Q_{e,j})$$
(31)

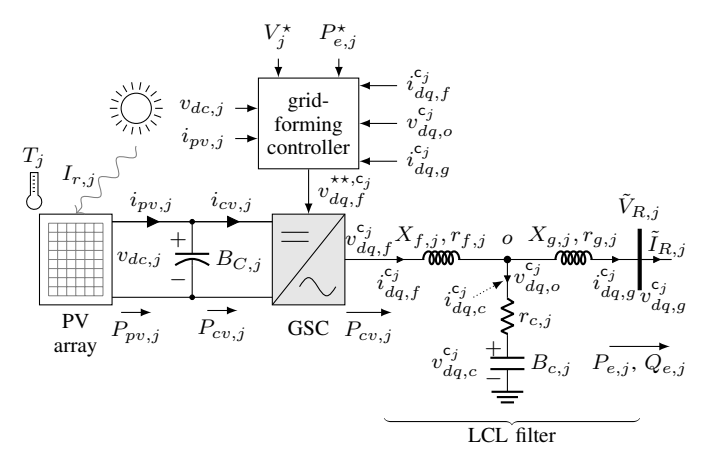


Fig. 2. Aggregated representation of a PV power plant.

which are respectively filtered active and reactive power:

$$P_{e,j} = v_{d,g}^{\mathsf{c}_j} i_{d,g}^{\mathsf{c}_j} + v_{q,g}^{\mathsf{c}_j} i_{q,g}^{\mathsf{c}_j}, Q_{e,j} = v_{q,g}^{\mathsf{c}_j} i_{d,g}^{\mathsf{c}_j} - v_{d,g}^{\mathsf{c}_j} i_{q,g}^{\mathsf{c}_j} \quad (32)$$

and are illustrated in Fig. 2.

For control, we also define a filtered version of  $i_{dq,g}^{c_j}$ :

$$\frac{d\widetilde{i}_{dq,g}^{\mathbf{c}_{j}}}{dt} = \frac{1}{\tau_{g,j}} \left( -\widetilde{i}_{dq,g}^{\mathbf{c}_{j}} + i_{dq,g}^{\mathbf{c}_{j}} \right) \tag{33}$$

which physically exists to filter grid transients.

# B. Converter Reference Frame

The angular speed of the reference frame  $c_i$  is [8]:<sup>2</sup>

$$\omega_{\mathsf{c}_{i}} = 1 - k_{p,j} (\widetilde{P}_{e,j} - \widetilde{P}_{e,j}^{\star}). \tag{34}$$

with  $\widetilde{P}_{e,i}$  from (30) and:

$$\frac{d}{dt}\widetilde{P}_{e,j}^{\star} = \frac{1}{\tau_{\omega,j}} \left( -\widetilde{P}_{e,j}^{\star} + P_{e,j}^{\star} - \max\{\Delta P_{e,j}^{\star}, 0\} \right) \tag{35}$$

for filtering  $P_{e,j}^{\star} - \max\{\Delta P_{e,j}^{\star}, 0\}$ . The command  $\Delta P_{e,j}^{\star}$  innovates the classical droop control law of [8] to modulate  $P_{cv,j}$  of (28). This to prevent dc-link voltage collapse as a result of imbalances between  $P_{pv,j}$  and  $P_{cv,j}$  which will be further explained in Section IV-B.

We note from (7) that  $\omega_{c_j}$  yields  $\theta_{c_j}$  ( $\nu = c_j$ ). The dynamics of the relative angle of the *j*-th renewable power plant are:

$$\frac{d}{dt}\delta_{\mathsf{c}_j} = \omega_b(\omega_{\mathsf{c}_j} - \omega_{\mathsf{e}}) \tag{36}$$

because  $d\delta_{c_j}/dt = d(\theta_{c_j} - \theta_e)/dt$ . Please, note the definition of  $d\theta_{c_j}/dt$  appears in (7) when  $\nu = c_j$ , for example. Nevertheless, the model of (36) requires  $\omega_e$  which is not defined for grids with machines and grid-forming converters with droop controllers. In a machine-based grid,  $\omega_e$  is the speed of a fictitious center of inertia [27]–[29].

# C. Speed of Synchronous Reference Frame

We define  $\omega_e$  for grids with a mix of machines and grid-forming converters with speed-droop control laws [8].

Proposition 1: The angular speed for the e frame is:

$$\omega_{e} = \frac{\sum_{i=1}^{I} \omega_{r_{i}} H_{r_{i}} + \sum_{j=1}^{J} \omega_{c_{j}} H_{c_{j}}}{\sum_{i=1}^{I} H_{r_{i}} + \sum_{j=1}^{J} H_{c_{j}}}$$
(37)

where  $H_{r_i}$  and  $\omega_{r_i}$  are in (14) as well as:

$$H_{\mathsf{c}_j} \triangleq \frac{\tau_{s,j}}{2k_{p,j}} \tag{38}$$

is a inertia constant of a *j*-th converter and  $\omega_{c_i}$  in (34).

*Proof:* We leverage the exposition of [28, p. 79] and [37]. From (30) and (34) by considering that  $\widetilde{P}_{e,j}^{\star}$  is constant:

$$\frac{d}{dt}\omega_{\mathbf{c}_{j}} = -\kappa_{p,j}\frac{d}{dt}\widetilde{P}_{e,j} = \frac{1}{2}\frac{2\kappa_{p,j}}{\tau_{s,j}}(\widetilde{P}_{e,j} - P_{e,j}). \tag{39}$$

Defining  $H_{\text{c}_j} = au_{s,j}/(2\kappa_{p,j})$  and applying addition of (39)  $\forall j$ :

$$\frac{d}{dt} \sum_{j=1}^{j=J} 2H_{c_j} \omega_{c_j} = \sum_{j=1}^{j=J} (\widetilde{P}_{e,j} - P_{e,j}). \tag{40}$$

The same approach is applied to (14)  $\forall i$  by considering that  $P_{m,i} \approx T_{m,i}$  and  $P_{e,i} \approx T_{e,i}$  in per unit to obtain:

$$\frac{d}{dt} \sum_{i=1}^{i=I} 2H_{r_i} \omega_{r_i} = \sum_{i=1}^{i=I} (P_{m,i} - P_{e,i}). \tag{41}$$

Because the addition of the right hand sides of (40) and (41) defines the mean acceleration or deceleration power of  $\omega_e$ :

$$2H_{e}\frac{d}{dt}\omega_{e} = \sum_{i=1}^{j=J} (\tilde{P}_{e,j} - P_{e,j}) + \sum_{i=1}^{j=I} (P_{m,i} - P_{e,i}).$$
 (42)

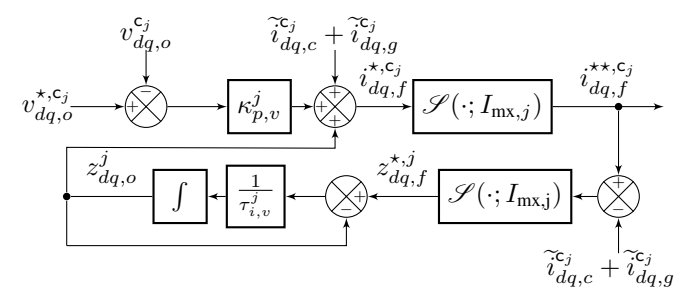
Here  $H_e \triangleq \sum_{i=1}^{i=I} H_{r_i} + \sum_{j=1}^{j=J} H_{c_j}$  is the inertia of a fictitious rotor spinning at  $\omega_e$ . Equation (37) arises by respectively substituting the left-hand sides of (40) and (41) into the right-hand sides of (42) and comparing terms.

Corollary 1: The angular speed of the e frame of a power grid with only grid-forming power converters satisfies:

$$\omega_{e} = \frac{\sum_{j=1}^{J} H_{c_{j}} \omega_{c_{j}}}{\sum_{j=1}^{J} H_{c_{i}}}.$$
 (43)

We briefly illustrate the magnitude of (38) for a 100-MVA PV power plant. Typically,  $\tau_{s,j}=1/(2\pi\cdot 30)$  s  $\approx 0.005$  s and  $k_{p,j}=0.05$  p.u. in the 100-MVA base [38], hence  $H_{c_j}\approx 0.05$  s from (38). This calculation shows that the inertia constant of a PV plant with grid-forming controls is not zero. We note here that it has been previously recognized that droop-control has nearly no inertia [39], but it has not been quantified. Here, the inertia value by droop control is calculated with (38). If inverters with virtual synchronous machine control are used [40], [41], their virtual inertia constants can be treated in (37) as if they were from actual synchronous machines [42]. Hence, definition (37) is valid for power systems with synchronous machines as well as for inverters steered by virtual synchronous machine and droop controls. We emphasize that (43) can be applied to grids

<sup>&</sup>lt;sup>2</sup>We note  $\omega_{c_i}$  is computed within a controller, it is not speed of a rotor.



(a) voltage regulator

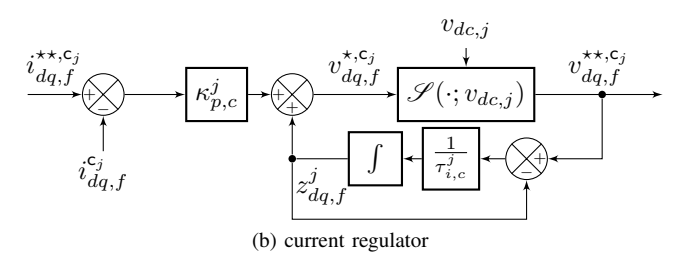


Fig. 3. Diagrams of voltage and current regulators for a PV power plant.

powered only by inverters with droop controls because  $H_{c_i}$ of (38) is not zero. However, if it is arbitrarily assumed that  $H_{c_j} = 0$ , that creates a conundrum in the calculation.

# D. Grid-Forming Strategy

We leverage the voltage control strategy for currentregulated PWM converters in [30]. We incorporate to this controller two-axis anti-windup proportional-integral (PI) regulators. Anti-windup technology [31, p. 91] is instrumental here to bound control commands and the flow of the integrator states in PI regulators, e.g., to ride through faults. The heart of the implemented grid-forming strategy for Fig. 2 is illustrated in Fig. 3. They are extensions from the one-axis (or onevariable) anti-windup series implementation in [31, p. 91] to two-axis systems. In particular, note in Fig. 3 that the control outputs of the two-axis PI regulators are bounded by a circle

via  $\mathscr S$  of (11) as explained in Section II-C using Fig. 1. The voltage controller drives  $v_{dq,o}^{c_j} \to v_{dq,o}^{\star,c_j}$ , q.v. (27), where:

$$v_{d,o}^{\star,c_j} = V_i^{\star} + k_{q,j} \widetilde{i}_{q,q}^{c_j}, \text{ and } v_{q,o}^{\star,c_j} = 0$$
 (44)

are dq-axis voltage set points. Here,  $V_i^{\star}$  and  $k_{q,j}$  are voltage magnitude command and voltage droop constant, respectively. Voltage control in Fig. 3a is achieved via the following dq PI regulator with two-axis anti-windup capability:

$$i_{dq,f}^{\star,c_{j}} = \kappa_{p,v}^{j} (v_{dq,o}^{\star,c_{j}} - v_{dq,o}^{c_{j}}) + z_{dq,o}^{j} + \tilde{i}_{dq,g}^{c_{j}} + \tilde{i}_{dq,c}^{c_{j}}$$
(45)  
$$i_{dq,f}^{\star,c_{j}} = \mathcal{S}(i_{dq,f}^{\star,c_{j}}, I_{\text{mx},j})$$
(46)

$$i_{dq,f}^{\star\star,c_j} = \mathcal{S}(i_{dq,f}^{\star,c_j}, I_{\text{mx},j})$$
(46)

$$z_{dq,f}^{\star,j} = \mathcal{S}(i_{dq,f}^{\star\star,c_j} - \tilde{i}_{dq,c}^{c_j} - \tilde{i}_{dq,g}^{c_j}, I_{\text{mx},j})$$

$$(47)$$

$$\frac{dz_{dq,o}^{j}}{dt} = \frac{1}{\tau_{i,v}^{j}} \left( -z_{dq,o}^{c_{j}} + z_{dq,f}^{\star,j} \right) \tag{48}$$

$$\widetilde{i}_{dq,c}^{\mathsf{c}_j} = -\omega_{\mathsf{c}_j} B_{c,j} v_{qd,c}^{\mathsf{c}_j} \tag{49}$$

which is illustrated in Fig. 3a. The voltage  $v_{qd,c}^{c_j}$  for (49) is calculated using (27). The parameters  $\kappa_{p,v}^j$  and  $\tau_{i,v}^j$  are

respectively the proportional and integration-time constants. The speed currents,  $i_{dq,c}^{c_j}$ , in (49) for (45) mitigates the impact of current circulation in the ac capacitors of the LCL filter in Fig. 2;  $v_{dq,c}^{c_j}$  is from (26). Similarly, the grid-currents,  $i_{dq,g}^{c_j}$ in (45) which are defined in (33) compensate for impacts from the grid. We note that  $\widetilde{i}_{dq,c}^{c_j}$  and  $\widetilde{i}_{dq,g}^{c_j}$  are respectively added and subtracted in (45) and (47) to not impact the PI integrators when saturation in (46) does not occur. The states of the PI integrators in (48) do not windup because the command  $z_{dq,f}^{\star,\jmath}$ is bounded in an origin-centered circle of radius  $I_{\text{mx},j}$  in (46), q.v. Fig. 1. Hence, the anti-windup functionality in (46)-(48) prevents overrated current commands during faults while automatically stopping integration. Further, the anti-windup functionality does not impact control directionality to not challenge synchronism, q.v. Fig. 1. In (46),  $I_{\text{mx},i} = S_i/S_b$ where  $S_j$  is the plant MVA rating.

The dq-axis current commands  $i_{dq,f}^{\star\star,c_j}$  in (46) are inputs to the following two-axis anti-windup PI current regulator:<sup>3</sup>

$$v_{dq,f}^{\star,c_{j}} = \kappa_{p,c}^{j} (i_{dq,f}^{\star\star,c_{j}} - i_{dq,f}^{c_{j}}) + z_{dq,f}^{j}$$

$$v_{da,f}^{\star\star,c_{j}} = \mathcal{S}(v_{da,f}^{\star,c_{j}}, v_{dc,j})$$
(50)

$$v_{dq,f}^{\star\star,\mathsf{c}_{j}} = \mathscr{S}(v_{dq,f}^{\star,\mathsf{c}_{j}}, v_{dc,j}) \tag{51}$$

$$\frac{dz_{dq,f}^j}{dt} = \frac{1}{\tau_{i,c}^j} \left( -z_{dq,f}^j + v_{dq,f}^{\star\star,c_j} \right) \tag{52}$$

which is depicted in Fig. 3b. The parameters  $\kappa_{p,c}^{j}$  and  $\tau_{i,c}^{j}$  are respectively the proportional and integration-time constants. The commands  $v_{dq,f}^{\star\star,c_j}$  of (51) are passed to the GSC of Fig. 2 to synthesize, e.g., via space-vector modulation [43, p. 485], the following voltages:

$$v_{dq,f}^{\mathsf{c}_j} = v_{dq,f}^{\star\star,\mathsf{c}_j} \tag{53}$$

which are applied to (25). We note that  $v_{dq,f}^{\star,c_j}$  in (51) are constrained within a circle of radius  $v_{dc,j}=\sqrt{E_{dc,j}};\,E_{dc,j}$  is in (28). This models modulation index limits that commonly appear in space-vector modulation [43, p. 487].<sup>4</sup>

Significant saturation of  $v_{dq,f}^{\star,c_j}$  can occur in (51) when the dc-link voltage  $v_{dc,j}$  considerably drops. This can in turn cause current controllability problems, q.v. (53). In particular, please note in (28) that a persistent  $P_{pv,j} < P_{cv,j}$  can lead to a deleterious drop in  $E_{dc,j}$ . The latter could happen when solar irradiance unexpectedly reduces during daylight operation. To describe these challenging conditions, we model the PV array in Subsection III-E. We also design a dc-link protection strategy in Section IV to prevent GSC controllability problems, which is also a novelty in this paper.

## E. Photovoltaic Array

We provide brief details of the PV array model in Fig. 4 which is adapted from [44, Fig. 4]. In Fig. 4: (i)  $R_{s,j} > 0$ and  $R_{sh,j} > 0$  are series and shunt resistances; (ii)  $v_{d,j}$ ,  $i_{d,j}$ , and  $i_{g,j}$  are per-unit diode voltage, diode current, and light

<sup>3</sup>We do not use feed-forward voltages in the current controller to not cancel out the impact of  $X_{f,j}$  in Fig. 2 as to mimic the reactances of synchronous machines, e.g., see  $(X_{d,i}-X_{d,i}')$  in (12) and  $(X_{q,i}-X_{q,i}')$  in (13).

<sup>4</sup>The  $\sqrt{3}$  from [43, p. 487] does not appear in (51) because voltage quantities are in per unit. Hence, the GSC modulates via (53) only voltages that satisfy  $\mathcal{M}(v_{dq,f}^{\star\star,c_j}) < v_{dc,j}$  [43, p. 487];  $\mathcal{M}$  is in (10).

generated current, respectively. This model considers uniform irradiance and temperature throughout several PV modules.

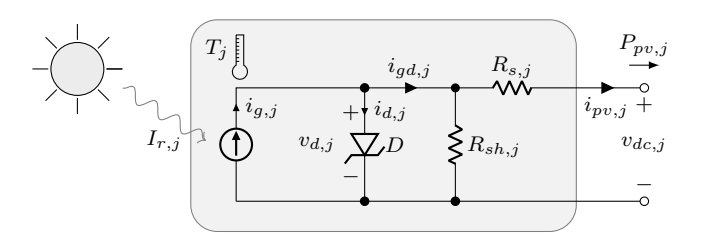


Fig. 4. Abstract model of j-th PV array.

The current  $i_{g,j}$  is proportional to solar irradiance  $I_{r,j}$ :

$$i_{g,j} = i_{g,j}^{\text{rated}} \times \frac{I_{r,j}}{I_{r,j}^{\text{std}}} > 0$$
 (54)

where  $i_{g,j}^{\rm rated}$  is rated light generated current during standard solar irradiance  $I_{r,j}^{\rm std}=1000$  W/m². The per-unit current through the module's internal diode satisfies [44]:

$$i_{d,j} = i_{0,j} \left( e^{\frac{v_{d,j}}{v_{T,j}}} - 1 \right)$$
 (55)

$$v_{d,j} = \frac{R_{sh,j}}{R_{s,j} + R_{sh,j}} \left( v_{dc,j} + R_{s,j} i_{g,j} - R_{s,j} i_{d,j} \right)$$
 (56)

$$i_{gd,j} = i_{g,j} - i_{d,j} \text{ and } v_{dc,j} \ge 0, i_{d,j} \ge 0.$$
 (57)

Here  $i_{0,j}$  and  $v_{d,j}$  are reverse saturation current and diode voltage, respectively. The voltage  $v_{T,j}$  is temperature voltage [44]. The power at the terminals of the PV array in Fig. 4 is:

$$P_{pv,j} = v_{d,j} i_{gd,j} - R_{s,j} \left( i_{gd,j} - \frac{v_{d,j}}{R_{sh,j}} \right)^2 - \frac{v_{d,j}^2}{R_{sh,j}}$$
 (58)

which is concave in  $v_{d,j}$  for fixed  $i_{g,j}$ .

Lemma 1:  $P_{pv,j}$  of (58) is concave in  $v_{d,j}$ .

*Proof:* We demonstrate this by: (i) determining concavity of each term of (58) and (ii) noting that sum of concave functions is concave [45, p. 79]. From (55) and (57), the term:

$$v_{d,j}i_{gd,j} = v_{d,j} \left( i_{g,j} + i_{0,j} \right) - i_{0,j}v_{d,j} \mathrm{e}^{\frac{v_{d,j}}{v_{T,j}}}$$

is concave because  $v_{d,j} \mathrm{e}^{v_{d,j}/v_{T,j}}$  is convex. The term  $i_{gd,j} - v_{d,j}/R_{sh,j}$  is concave, hence  $-R_{s,j} \left(i_{gd,j} - v_{d,j}/R_{sh,j}\right)^2$  is as well. Finally,  $-v_{d,j}^2/R_{sh,j}$  is a parabola opening downwards.

To obtain  $P_{pv,j}$  in (58) for (28), it is necessary to calculate an  $i_{d,j}$  and a  $v_{d,j}$  that satisfies (55) and (56). The aforementioned implicit relationship has to be numerically solved. Thus, we compute at each time-step of a simulation,  $i_{d,j}$  such that:

$$H(i_{d,j}, v_{dc,j}, i_{g,j}) = i_{d,j} - i_{0,j} \left( e^{\frac{v_{d,j}}{v_{T,j}}} - 1 \right) = 0$$
 (59)

with  $v_{d,j}$  of (56) using the following Newton-Rapson iterates:

$$i_{d,j,\ell+1} = i_{d,j,\ell} - \frac{H(i_{d,j,\ell}, v_{dc,j,\ell}, i_{g,j,\ell})}{H'(i_{d,j,\ell}, v_{dc,j,\ell}, i_{g,j,\ell})}$$
(60)

for  $\ell = 0, 1, 2, \ldots$  where H' is the derivative of H with respect to  $i_{d,j}$ . These iterates always converge in a few steps to a unique solution regardless of the initial guess  $i_{d,j,0}$  [36], hence it is a sound numerical implementation.

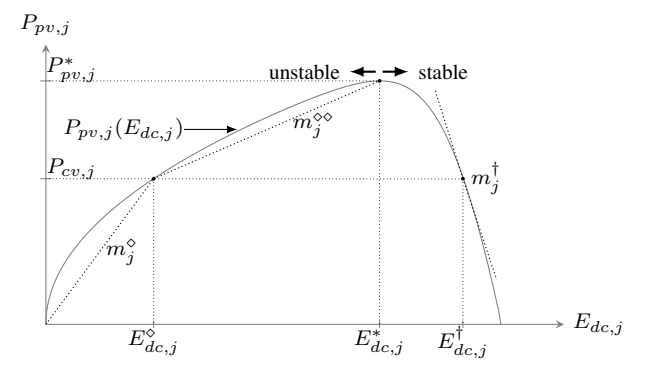


Fig. 5. PV array power versus dc-link energy curve for proof of stability of equilibrium points in Section III-F.

# F. Analysis of Dc-link Stability

The maximum power a PV array can source,  $P_{pv,j}=P_{pv,j}^*$ , is unique because of the concavity of  $P_{pv,j}$ , q.v. Lemma 1. Hence, we write  $P_{pv,j}^*=P_{pv,j}(E_{dc,j}^*)$  because  $P_{pv,j}$  is also concave in  $v_{dc,j}$  and  $E_{dc,j}=v_{dc,j}^2$ . Here,  $E_{dc,j}^*$  is optimal dc-link capacitor energy.

Lemma 2:  $P_{pv,j}$  of (58) is concave in  $v_{dc,j}$  and  $E_{dc,j}$ .

*Proof:* We write  $v_{dc,j} = g(v_{d,j})$  with g from (55) and (56) which is convex and strictly increasing on  $v_{d,j}$ . Hence,  $v_{d,j} = g^{-1}(v_{dc,j})$  is concave [46, p. 10]. Because  $P_{pv,j}(v_{d,j})$  is concave, so is the function composition  $P_{pv,j}(g^{-1}(v_{dc,j}))$  [45, p. 85].  $P_{pv,j}$  of (58) is concave in  $E_{dc,j}$  because  $E_{dc,j} = v_{dc,j}^2$ .

The concavity of  $P_{pv,j}$  in  $E_{dc,j}$ , shown in Fig. 5, implies the following possible equilibrium points for (28):

- 1) If  $P_{cv,j} < P_{pv,j}^*$ ,  $\exists E_{dc,j}^{\dagger} > E_{dc,j}^*$  such that  $P_{cv,j} = P_{pv,j}(E_{c,j}^{\dagger})$ .
- $P_{pv,j}(E_{dc,j}^{\dagger}).$ 2) If  $P_{cv,j} < P_{pv,j}^*$ ,  $\exists E_{dc,j}^{\diamond} < E_{dc,j}^*$  such that  $P_{cv,j} = P_{pv,j}(E_{dc,j}^{\diamond}).$
- 3) If  $P_{cv,j} > P_{pv,j}^*$ ,  $\not\equiv E_{dc,j}$  such that  $P_{cv,j} = P_{pv,j}(E_{dc,j})$ . We note in Fig. 5 that the concavity of  $P_{pv,j}$  in  $E_{dc,j}$  suggests the following physical notions. Assume  $P_{pv,j} = P_{cv,j}$  in (28) which occurs when  $E_{dc,j} = E_{dc,j}^{\dagger}$  and  $E_{dc,j} = E_{dc,j}^{\dagger}$ . The increase of  $P_{cv,j}$  in (28) causes the decrease of  $E_{dc,j}$  from  $E_{dc,j}^{\dagger}$  that signifies the *increase* of  $P_{pv,j}$ . This is a stable behavior because  $P_{pv,j}$  increases to compensate the increase of  $P_{cv,j}$  by the GSC in Fig. 2. On the other hand, the increase of  $P_{cv,j}$  causes the decrease of  $E_{dc,j}$  from  $E_{dc,j}^{\diamond}$  that signifies the *decrease* of  $P_{pv,j}$ . This is an unstable behavior because  $P_{pv,j}$  decreases in lieu of increasing to compensate  $P_{cv,j}$ .

Theorem 1: Let  $E_{dc,j}^{\dagger} > E_{dc,j}^{*}$  and  $P_{pv,j}^{*} > P_{cv,j}$ . Also, let  $E_{dc,j}^{\diamond} < E_{dc,j}^{*}$  and  $P_{pv,j}^{*} > P_{cv,j}$ . If  $P_{cv,j} = P_{pv,j}(E_{dc,j}^{\dagger}) = P_{pv,j}^{\dagger}$ , then  $E_{dc,j}^{\dagger}$  is an stable equilibrium of (28). If  $P_{cv,j} = P_{pv,j}(E_{dc,j}^{\diamond})$ , then  $E_{dc,j}^{\diamond}$  is an unstable equilibrium of (28).

*Proof:* To prove stability of  $E_{dc,i}^{\dagger}$ , consider (q.v. Fig. 5):

$$P_{pv,j}(E_{dc,j}) < m_j^{\dagger}(E_{dc,j} - E_{dc,j}^{\dagger}) + P_{pv,j}(E_{dc,j}^{\dagger})$$
 (61)

for  $E_{dc,j} \in (E_{dc,j}^*, E_{dc,j}^{\dagger}) \cup (E_{dc,j}^{\dagger}, \infty)$ , respectively. Here,  $m_j^{\dagger} = dP_{pv,j}/dE_{dc,j} \leq 0$  because of Lemma 2. Also, consider a continuously differentiable function:

$$V(E_{dc,j}) = \frac{1}{2} (E_{dc,j} - E_{dc,j}^{\dagger})^2$$
 (62)

which is commonly used to ascertain local stability [47, p. 114]. From (28) and (61), one can infer that:

$$\frac{d}{dt}E_{dc,j} < \frac{m_j^{\dagger}}{B_{C,j}}(E_{dc,j} - E_{dc,j}^{\dagger}). \tag{63}$$

By considering (62) and (63), one obtains:

$$\frac{d}{dt}V(E_{dc,j}) = (E_{dc,j} - E_{dc,j}^{\dagger})\frac{d}{dt}E_{dc,j}$$
 (64)

$$\frac{d}{dt}V(E_{dc,j}) < \frac{m_j^{\dagger}}{B_{C,j}}(E_{dc,j} - E_{dc,j}^{\dagger})^2$$
 (65)

which establishes stability of  $E_{dc,j}^{\dagger}$  because  $m^{\dagger} \leq 0$ . To ascertain instability of  $E_{dc,j}^{\diamond}$ , we employ (q.v. Fig. 5):

$$P_{pv,j}(E_{dc,j}) > m_i^{\diamond}(E_{dc,j} - E_{dc,j}^{\diamond}) + P_{pv,j}(E_{dc,j}^{\diamond})$$
 (66)

$$P_{pv,j}(E_{dc,j}) > m_j^{\diamond \diamond}(E_{dc,j} - E_{dc,j}^{\diamond}) + P_{pv,j}(E_{dc,j}^{\diamond}) \tag{67}$$

where  $m_j^{\diamond} = P_{pv,j}^{\diamond}/E_{dc,j}^{\diamond} > 0$  and  $m_j^{\diamond \diamond} = (P_{pv,j}^* - P_{pv,j}^{\diamond})/(E_{dc,j}^* - E_{dc,j}^{\diamond}) > 0$  because of Lemma 2; here  $P_{pv,j}^{\diamond} = P_{pv,j}(E_{dc,j}^{\diamond})$ . The inequalities (66) and (67) are respectively valid for  $E_{dc,j} \in (0, E_{dc,j}^{\diamond})$  and  $E_{dc,j} \in$  $(E_{dc,j}^{\diamond}, E_{dc,j}^{*})$ . Application of (66) and (67) in (28) leads to:

$$\frac{d}{dt}E_{dc,j} > \frac{m_j^{\diamond}}{B_{C,j}}(E_{dc,j} - E_{dc,j}^{\diamond}) \tag{68}$$

$$\frac{d}{dt}E_{dc,j} > \frac{m_j^{\diamond \diamond}}{B_{C,i}}(E_{dc,j} - E_{dc,j}^{\diamond}) \tag{69}$$

which applied to  $dV(E_{dc,j})/dt = (E_{dc,j} - E_{dc,j}^{\diamond})dE_{dc,j}/dt$ respectively produce:

$$\frac{d}{dt}V(E_{dc,j}) > \frac{m_j^{\diamond}}{B_{C,j}}(E_{dc,j} - E_{dc,j}^{\diamond})^2$$
 (70)

$$\frac{d}{dt}V(E_{dc,j}) > \frac{m_j^{\diamond \diamond}}{B_{C,i}}(E_{dc,j} - E_{dc,j}^{\diamond})^2 \tag{71}$$

for  $E_{dc,j} \in (0, E_{dc,j}^{\diamond})$  and  $E_{dc,j} \in (E_{dc,j}^{\diamond}, E_{dc,j}^{*})$ . This establishes instability of  $E_{dc,j}^{\diamond}$  because  $m_{j}^{\diamond} > 0$  and  $m_{j}^{\diamond \diamond} > 0$ .

The aforementioned theorem implies that a stable gridforming operation can be reached only when  $E_{dc,j} > E_{dc,j}^*$ . However, if  $E_{dc,j} < E_{dc,j}^*$ , the dynamics of the PV array do not have stable equilibria which is detrimental for gridforming operation. This can occur if solar irradiance drops; hence, dc-link voltage protection is needed.

# IV. DC-LINK VOLTAGE PROTECTION

To stimulate the dc-link voltage protection, we estimate  $E_{dc,j}^*$  and  $P_{pv,j}^*$  which is the maximum power point (MPP) of a PV array. This process uses the abstract model of the PV array in Section III-E as well as voltage  $v_{dc,j}$  and current  $i_{pv,j}$ , q.v. Fig. 2. Estimated quantities are represented with hats.

# A. Estimation of Optimal Dc-link Voltage

We first estimate  $i_{g,j}$  of (54) which yields  $I_{r,j}$  of (54) with:

$$\widehat{v}_{d,j} = v_{dc,j} + R_{s,j} i_{pv,j}, \, \widehat{i}_{d,j} = i_{0,j} \left( e^{\frac{\widehat{v}_{d,j}}{v_{T,j}}} - 1 \right)$$
 (72)

$$\widehat{i}_{g,j} = \widehat{i}_{d,j} + \widehat{i}_{sh,j} + i_{pv,j} \text{ and } \widehat{i}_{sh,j} = \widehat{v}_{d,j}/R_{sh,j}. \tag{73}$$

We then estimate the optimal dc-link voltage  $\hat{v}_{dc,i}^*$  which yields  $\widehat{E}_{dc.i}^*$  for Section IV-B. To that end, we define:

$$i_{gd,j} = \hat{i}_{g,j} - i_{d,j} \tag{74}$$

with  $\hat{i}_{q,j}$  from (73) for usage in (58). Because (58) is concave on  $v_{d,j}$ , q.v. Lemma 2, there is a unique  $\hat{v}_{d,j}^*$  such that  $P_{pv}(\widehat{v}_{d,j}^*)$  is maximum and  $dP_{pv}(v_{d,j})/dv_{d,j}=\widehat{0}$  when  $v_{d,j} = \hat{v}_{d,j}^*$ . Hence, to calculate  $\hat{v}_{d,j}^*$ , we find a zero of:

$$\begin{split} & \frac{d}{dv_{d,j}} P_{pv}(v_{d,j}) \triangleq G(v_{d,j}) = i_{gd,j} + v_{d,j} \frac{d}{dv_{d,j}} i_{gd,j} - \\ & 2R_{s,j} \left( i_{gd,j} - \frac{v_{d,j}}{R_{sh,j}} \right) \left( \frac{d}{dv_{d,j}} i_{gd,j} - \frac{1}{R_{sh,j}} \right) - \frac{2v_d}{R_{sh,j}} \,. \end{split}$$

with  $i_{d,j}$  from (55). This is efficiently done (in the sense of number of computations) by using Newton-Raphson iterations:

$$v_{d,j,p+1} = v_{d,j,p} - \frac{G(v_{d,j,p})}{G'(v_{d,j,p})}$$
(76)

for  $p = 0, 1, 2, \dots$  where G is from (75) and G' is the derivative of G. In G and G' of (76), we use:

$$\frac{d}{dv_{d,j}}i_{gd,j} = -\frac{i_{0,j}}{v_{T,j}}e^{\frac{v_{d,j}}{v_{T,j}}} \text{ and } \frac{d^2}{dv_{d,j}^2}i_{gd,j} = -\frac{i_{0,j}}{v_{T,j}^2}e^{\frac{v_{d,j}}{v_{T,j}}}.$$
(77)

The iterations of (76) end if  $|v_{d,j,p+1} - v_{d,j,p}|/|v_{d,j,p}| < \epsilon_{\text{tol}}$ with  $\epsilon_{\text{tol}}$  a relative tolerance when  $|v_{d,j,p}| > 0$ . If the iterations terminate at  $p^* = p + 1$ , then  $\hat{v}_{d,j}^* = v_{d,j,p^*}$ .

Lemma 3: If the starting point  $v_{d,i,0}$  for (76) satisfies:

$$v_{d,j,0} > \frac{2R_{s,j}\hat{i}_{g,j}v_{T,j} - 3av_{T,j}^2 - 6R_{s,j}i_{0,j}v_{T,j}}{av_{T,j} + 8R_{s,i}i_{0,j}}$$
(78)

with  $a = 1 + 2R_{s,j}/R_{sh,j}$ , the iterations therein converge.

*Proof:* By ascertaining the domain of  $v_{d,j}$  on which G of (75) is decreasing and concave [48, p. 86].  $G(v_{d,j})$ of (75) is decreasing because of the concavity of  $P_{pv}(v_{d,i})$ , q.v. Lemma 1. Equation (78) arises by studying the domain of  $v_{d,j}$  that makes  $G''(v_{d,j}) > 0$  after application of Taylor's theorem; G'' is the second derivative of G in (75).

The voltage  $\hat{v}_{dc,j}^*$  is calculated by solving (56) for  $v_{dc,j}$  and substitution of  $v_{d,j}=\widehat{v}_{d,j}^*$  and  $i_{gd,j}=\widehat{i}_{g,j}-i_{0,j}(\mathrm{e}^{\widehat{v}_{d,j}^*/v_{T,j}}-1)$ with  $\widehat{i}_{g,j}$  from (73). Thus,  $\widehat{E}^*_{dc,j} = \max\{(\widehat{v}^*_{dc,j})^2, (v_{\text{mn},j})^2\}$ for Section III-F. Here, we consider the minimum input voltage,  $v_{\text{mn},j}$ , the GSC of Fig. 2 requires to operate, q.v. [49]. This is useful to study full outages of solar irradiance.

## B. Active Dc-link Voltage Protection

We explain how to regulate  $\Delta P_{e,j}^{\star}$  in (35) for dc-link voltage protection. The main idea is to actively control  $P_{cv,j}$  of (28) and (29) by steering  $\Delta P_{e,j}^{\star}$  which impacts  $\omega_{c_j}$  of (34). We note in (28) that control of  $E_{dc,j}$  is challenging because: (i)  $P_{pv,j}$  is concave in  $E_{dc,j}$  (q.v. Lemma 2) and (ii) has a saddle point at  $E_{dc,j} = E_{dc,j}^* \approx \widehat{E}_{dc,j}^*$ . We recall  $\widehat{E}_{dc,j}^* = (\widehat{v}_{dc,j}^*)^2$  is estimated in Section IV-A. As done in control of concave systems [50], we use two control errors:

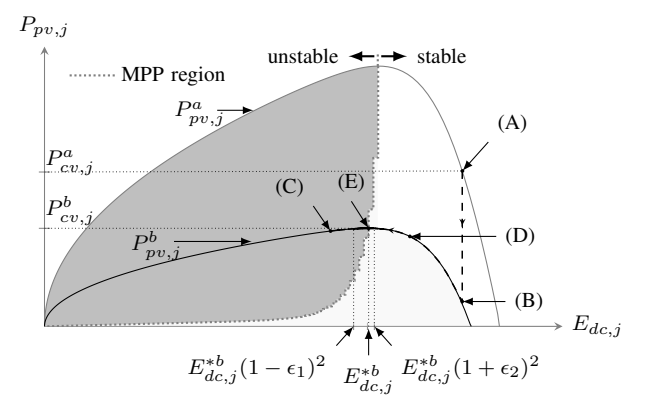


Fig. 6. Behavior of PV array power versus dc-link energy during solar irradiance disturbances.

$$e_{dc1,j} = k_{pp,j} \left( \widehat{E}_{dc,j}^* (1 - \epsilon_1)^2 - E_{dc,j} \right)$$
 (79)

$$e_{dc2,j} = k_{pp,j} \left( \widehat{E}_{dc,j}^* (1 + \epsilon_2)^2 - E_{dc,j} \right).$$
 (80)

to regulate  $\Delta P_{e,j}^{\star}$  via a PI regulator with activation conditions:

$$\Delta P_{e,j}^{\star} = \begin{cases} e_{dc1,j} + z_{P_{e,j}} & \text{if } E_{dc,j} < \widehat{E}_{dc,j}^{\star} (1 - \epsilon_1)^2 \\ z_{P_{e,j}} & \text{otherwise} \end{cases}$$
(81)

$$\frac{d}{dt}z_{P_{e,j}} = \begin{cases}
\frac{e_{dc1,j}}{\tau_{pp,j}} & \text{if } E_{dc,j} < \widehat{E}_{dc,j}^* (1 - \epsilon_1)^2 \\
\frac{e_{dc2,j}}{0.5\tau_{pp,j}} & \text{if } E_{dc,j} > \widehat{E}_{dc,j}^* (1 + \epsilon_2)^2 \\
0 & \widehat{E}_{dc,j}^* \in \mathcal{D}_{dc,j} \\
0 & \text{if } z_{P_{e,j}} \ge P_{e,j}^* \text{ and } \widehat{E}_{dc,j}^* > E_{dc,j} \\
0 & \text{if } z_{P_{e,j}} \le 0 \text{ and } \widehat{E}_{dc,j}^* < E_{dc,j}.
\end{cases}$$
(82)

The set  $\mathcal{D}_{dc,j}=(\widehat{E}_{dc,j}^*(1-\epsilon_1)^2,\widehat{E}_{dc,j}^*(1+\epsilon_2)^2)$  defines a deadband to mitigate continuous chattering [50], [51]. The user-defined parameters  $\epsilon_1$  and  $\epsilon_2$  are relative small numbers. The PI-regulator parameters in (79)–(82) are determined with  $k_{pp,j}=B_{C,j}/(3\tau_{s,j})$  and  $\tau_{pp,j}=12\tau_{s,j}$  where  $B_{C,j}$  and  $\tau_{s,j}$  are from (28) and (30), respectively. The settling time of the controller is  $30\tau_{s,j}$ . We clarify that (81) and (82) are defined piecewise because  $P_{pv,j}$  is concave in  $E_{dc,j}$  as illustrated in Fig. 6. The ultimate goal is to prevent low dclink voltages that would impact (51) and cause, for example, synchronization problems. This is demonstrated via simulation in Section VI-B. We explain the operational rationale of (81) and (82) next.

In Fig. 5, let  $P^a_{pv,j}$  and  $P^b_{pv,j}$  be PV array power curves for two values of solar irradiance  $I^a_{r,j}$  and  $I^b_{r,j}$  ( $I^a_{r,j} > I^b_{r,j}$ ), respectively. Also assume that a PV array initially observes  $I^a_{r,j}$  and is operating at the stable equilibrium (A) in Fig. 5. Then, consider irradiance instantaneously drops to  $I^b_{r,j}$ , consequently, the PV array operation changes to point (B) where  $P^b_{pv,j} < P^a_{cv,j}$ . Thus,  $E_{dc,j}$  of (28) begins dropping because the grid-forming converter is not cognizant yet that  $P^b_{pv,j} < P^a_{cv,j}$  given that  $E_{dc,j} \ge \hat{E}^*_{dc,j} (1+\epsilon_2)^2$ . When  $(E_{dc,j}, P^b_{pv,j})$  reaches point (C) in Fig. 5, the error  $e_{dc1,j}$  of (79) causes: (i) an increase of  $\Delta P^*_{e,j}$  in (81), (ii) the reduction of  $\omega_{c,j}$  of (34) via (35), and (iii) the reduction of  $P_{cv,j}$  in (28). We recall that dc-link energy will not achieve a stable equilibrium in (C),

q.v. Theorem 1. Hence,  $E_{dc,j}$  is driven to point (D) in Fig. 5. At that point, the error  $e_{dc2,j}$  in (80) activates to steer the integrator state  $z_{P_{e,j}}$  in (82) towards zero. The aforementioned process can momentarily chatter until  $E_{dc,j} \in \mathcal{D}_{dc,j}$  where the PV array is close to the MPP, e.g., see point (E).

It is worth noting here that the proposed protection system does not cause de-rated operation of a PV power plant. In fact, it permits the GSC of Fig. 2 to transfer up to the maximum power that the PV array can produce at any point in time. If the protection activates, a disadvantage is that the PV inverter will not be able to participate in frequency regulation. This is analogous to a synchronous generating set in which its governor has reached its upper limit [28, Ch. 15].

## V. INTERCONNECTED POWER SYSTEM

We interconnect conventional power plants, PV power plants, and composite loads via a transmission system to form a set of DAEs as in (1)–(3).

# A. Dynamic Voltages Behind Impedances

For interconnection, the *i*-th power plant of Section II-D is viewed as a voltage source behind a transient impedance [29]:

$$\widetilde{V}_{G,i} = -(r_{s,i} + jX'_{d,i})\widetilde{I}_{G,i} + \widetilde{E}_{G,i}$$
 (83)

$$\widetilde{V}_{G,i} = e^{j\delta_{r_i}}(v_d^{r_i} + jv_q^{r_i}), \quad \widetilde{I}_{G,i} = e^{j\delta_{r_i}}(i_d^{r_i} + ji_q^{r_i})$$
(84)

$$\widetilde{E}_{G,i} = e^{\mathsf{j}\delta_{\mathsf{r}_i}} (e_d^{\mathsf{r}_i} + \mathsf{j}e_q^{\mathsf{r}_i}). \tag{85}$$

The phasors  $\widetilde{V}_{G,i}$ ,  $\widetilde{I}_{G,i}$ , and  $\widetilde{E}_{G,i}$  model terminal voltage, terminal current, and voltage behind transient impedance, respectively. The voltages  $v_{dq}^{r_i}$  are from (24). The dynamics of  $e_d^{r_i}$ ,  $e_q^{r_i}$ , and  $\delta_{r_i}$  are modeled in (12), (13), and (15), respectively. The phasor  $\widetilde{I}_{G,i}$  to determine  $i_d^{r_i}$  and  $i_q^{r_i}$  is modeled in Section V-C.

The voltage behind impedance of the *j*-th PV plant is [36]:

$$\widetilde{V}_{R,j} = -(r_{g,j} + r_{c,j} + jX_{g,j})\widetilde{I}_{R,j} + \widetilde{E}_{R,j}$$
 (86)

$$\widetilde{V}_{R,j} = e^{j\delta_{c_j}} (v_{d,q}^{c_j} + jv_{q,q}^{c_j}), \quad \widetilde{I}_{R,j} = e^{j\delta_{c_j}} (i_{d,q}^{c_j} + ji_{q,q}^{c_j})$$
 (87)

$$\widetilde{E}_{R,j} = \mathrm{e}^{\mathrm{j}\delta_{\mathbf{c}_{j}}} (e_{d,g}^{\mathbf{c}_{j}} + \mathrm{j}e_{q,g}^{\mathbf{c}_{j}}) \,, \quad e_{dq,g}^{\mathbf{c}_{j}} = r_{c,j} i_{dq,f}^{\mathbf{c}_{j}} + v_{dq,c}^{\mathbf{c}_{j}} \quad (88)$$

Here,  $i_{dq,f}^{c_j}$ ,  $v_{dq,c}^{c_j}$ , and  $\delta_{c_j}$  are from (25), (26), and (36). The phasors  $\widetilde{V}_{R,j}$ ,  $\widetilde{I}_{R,j}$ , and  $\widetilde{E}_{R,j}$  model terminal voltage, terminal current, and voltage behind impedance, respectively The phasor  $\widetilde{I}_{R,j}$  to calculate  $i_{dd,q}^{c_j}$  is in Section V-C.

#### B. Composite Loads

We model the k-th composite load (k = 1, ..., K) made of direct-drive motors, constant power demands, and constant impedances [52]–[54]. For motor loads, the relationship between bus voltage  $\widetilde{V}_{L,k}$  and motor current  $\widetilde{I}_{m,k}$  is [43, p. 238]:

$$\widetilde{V}_{L,k} = \left( (r_{s,k} + jX_{ls,k}) + \frac{jX_{M,k} \left( \frac{r'_{r,k}}{s_{m,k}} + jX_{lr,k} \right)}{jX_{M,k} + \left( \frac{r'_{r,k}}{s_{m,k}} + jX_{lr,k} \right)} \right) \widetilde{I}_{m,k}.$$
(89)

Here,  $s_{m,k}=(\omega_{\rm e}-\omega_{m,k})/\omega_{\rm e}$  is slip,  $\omega_{\rm e}$  is from (37), and:

$$\frac{d}{dt}\omega_{m,k} = \frac{1}{2H_{m,k}}(T_{e,k} - T_{m,k}). \tag{90}$$

Mechanical and electromagnetic torques in the k-th motor are:

$$T_{m,k} = K_{m,k}\omega_{m,k}^2 \text{ and } T_{e,k} = \frac{X_{M,k}^2 r'_{r,k} s_{m,k} |\widetilde{V}_{L,k}|^2}{\alpha_k^2 + \beta_k^2}$$
 (91)

respectively. Here,  $\alpha_k = r_{s,k}r'_{r,k} + s_{m,k}(X^2_{M,k} - X_{ss,k}X'_{rr,k})$  and  $\beta_k = (r'_{r,k}X_{ss,k} + s_{m,k}r_{s,k}X'_{rr,k})$ . The parameters  $r_{s,k}, r'_{r,k}, X_{M,k}, X_{ss,k}, X_{lr,k}, X'_{rr,k}, X_{ls,k}$  are per unit version of the ones defined in [43, p. 244].

The constant power and impedance load relationships are:

$$\operatorname{conj}\left(\widetilde{I}_{p,k}\right)\widetilde{V}_{L,k}+\left(P_{p,k}+\mathrm{j}Q_{p,k}\right)=0\tag{92}$$

$$\widetilde{V}_{L,k} + \widetilde{I}_{z,k} Z_k = 0 \tag{93}$$

with  $\operatorname{conj}(\cdot)$  a complex-conjugate operator. Here,  $\widetilde{I}_{p,k}$  and  $\widetilde{I}_{z,k}$  are current phasors by constant power and impedance loads. The variables  $P_{p,k}$ ,  $Q_{p,k}$ ,  $Z_k$  are real power, reactive power, and impedance, respectively. An example of a constant power load is a motor driven by a variable frequency drive [54]. We recall from (9) that the voltage and current phasors in (92) and (93) can be expressed in dq coordinates for computational purposes.

The current  $I_{L,k}$  of each k-th composite load satisfies:

$$\widetilde{I}_{L,k} + \widetilde{I}_{m,k} + \widetilde{I}_{p,k} + \widetilde{I}_{z,k} = 0.$$
(94)

# C. Transmission System

Currents injected by conventional and PV power plants as well as composite loads relate to terminal voltages by [29]:

$$\begin{bmatrix} \widetilde{I}_{G} \\ \widetilde{I}_{R} \\ \widetilde{I}_{L} \end{bmatrix} - \begin{bmatrix} Y_{GG}^{\gamma} & Y_{GR}^{\gamma} & Y_{GL}^{\gamma} \\ Y_{RG}^{\gamma} & Y_{RR}^{\gamma} & Y_{RL}^{\gamma} \\ Y_{LG}^{\gamma} & Y_{LR}^{\gamma} & Y_{LL}^{\gamma} \end{bmatrix} \begin{bmatrix} \widetilde{V}_{G} \\ \widetilde{V}_{R} \\ \widetilde{V}_{L} \end{bmatrix} = \mathbf{0}$$
(95)
$$\widetilde{F}_{Y} = [\widetilde{F}_{Y,1}, \widetilde{F}_{Y,2}, \dots]^{\top}$$
(96)

with  $\widetilde{F} \in \{\widetilde{V},\widetilde{I}\}$  a vector of voltage and current phasors. The index  $\chi \in \{G,R,L\}$  denotes conventional assets, renewable PV plants, and composite loads. The submatrices  $Y_{GG}^{\gamma}, Y_{GR}^{\gamma}, Y_{RG}^{\gamma}, Y_{RG}^{\gamma}, Y_{RR}^{\gamma}, Y_{RL}^{\gamma}, Y_{LG}^{\gamma}, Y_{LR}^{\gamma}$  and  $Y_{LL}^{\gamma}$  are partitions of the admittance matrix  $Y^{\gamma}$ . The network matrices are indexed by  $\gamma = \{1,2,3\}$  in (2) to model faults.

# D. Power System Model

In (1)–(3):  $\boldsymbol{x}^{\top} = [\boldsymbol{x}_{G}^{\top}, \boldsymbol{x}_{R}^{\top}, \boldsymbol{\omega}_{m}^{\top}], \ \boldsymbol{y}^{\top} = [\boldsymbol{y}_{G}^{\top}, \boldsymbol{y}_{R}^{\top}, \boldsymbol{y}_{L}^{\top}], \ \boldsymbol{u}^{\top} = [\boldsymbol{u}_{G}^{\top}, \boldsymbol{u}_{R}^{\top}], \ \boldsymbol{\Psi}^{\top} = [\boldsymbol{\Psi}_{G}^{\top}, \boldsymbol{\Psi}_{R}^{\top}, \boldsymbol{\Psi}_{L}^{\top}].$  The vector  $\boldsymbol{w} = [I_{r,1}, I_{r,2}, \ldots]^{\top}$  from (54). The vector  $\boldsymbol{x}$  is composed by:

$$\boldsymbol{x}_{G}^{\top} = [\boldsymbol{e}_{dq}^{\mathsf{r}\top}; \boldsymbol{\omega}_{\mathsf{r}}^{\top}; \boldsymbol{\delta}_{\mathsf{r}}^{\top}; \boldsymbol{T}_{m}^{\top}; \boldsymbol{P}_{v}^{\top}; \boldsymbol{e}_{fd}^{\top}; \boldsymbol{v}_{a}^{\top}; \boldsymbol{r}_{f}^{\top}] \in \mathbb{R}^{9I} \qquad (97)$$

$$\boldsymbol{x}_{R}^{\top} = [\boldsymbol{i}_{dq,f}^{\mathsf{c}\top}; \boldsymbol{v}_{dq,c}^{\mathsf{c}\top}; \boldsymbol{E}_{dc}^{\top}; \boldsymbol{\tilde{P}}_{e}^{\top}; \boldsymbol{\tilde{Q}}_{e}^{\top}; \boldsymbol{\tilde{P}}_{e}^{\star\top}; \\
\boldsymbol{\delta}_{\mathsf{c}}^{\mathsf{c}}; \boldsymbol{z}_{da,c}^{\top}; \boldsymbol{z}_{da,f}^{\top}; \boldsymbol{z}_{P_{e}}^{\top}] \in \mathbb{R}^{14J} \qquad (98)$$

We construct, for example, from (12), (13), and (25):

$$\mathbf{e}_{dq}^{\mathsf{r}\top} = [e_d^{\mathsf{r}_1}, e_q^{\mathsf{r}_1}, e_d^{\mathsf{r}_2}, e_q^{\mathsf{r}_2}, \dots, e_d^{\mathsf{r}_I}, e_q^{\mathsf{r}_I}] \tag{99}$$

$$\boldsymbol{i}_{dq,f}^{\mathsf{c}\mathsf{\top}} = [i_{d,f}^{\mathsf{c}_1}, i_{q,f}^{\mathsf{c}_1}, i_{d,f}^{\mathsf{c}_2}, i_{q,f}^{\mathsf{c}_2}, \dots, i_{d,f}^{\mathsf{c}_J}, i_{q,f}^{\mathsf{c}_J}] \tag{100}$$

The vectors in  $\boldsymbol{u}$  are:

$$\boldsymbol{y}_{R}^{\top} = [\boldsymbol{v}_{dq}^{\mathsf{r}\top}, \boldsymbol{i}_{dq}^{\mathsf{r}\top}], \boldsymbol{y}_{G}^{\top} = [\boldsymbol{v}_{dq,g}^{\mathsf{c}\top}, \boldsymbol{i}_{dq,g}^{\mathsf{c}\top}], \boldsymbol{y}_{L}^{\top} = [\boldsymbol{v}_{dq,L}^{\top}, \boldsymbol{i}_{dq,L}^{\top}]$$

$$(101)$$

TABLE I
PARAMETERS OF A PV PLANT IN ITS RATING BASE

Para.	Value	Unit	Description
$r_f$	0.0025	p.u.	filter inductor resistance
$X_f$	0.25	p.u.	filter inductor reactance
$r_g$	0.0012	p.u.	step-up transformer resistance
$X_g$	0.03	p.u.	step-up transformer reactance
$r_c$	0.04	p.u	filter capacitor resistance
$B_c$	0.24	p.u.	filter capacitor susceptance
$B_C$	0.036	p.u.	normalized dc-link capacitance
$i_0$	$7.165 \times 10^{-13}$	p.u.	reverse saturation current
$R_s$	0.0731	p.u.	series resistance of PV array
$R_{sh}$	58	p.u.	shunt resistance of PV array

TABLE II
CONTROL PARAMETERS OF A PV PLANT IN ITS RATING BASE

Para.	Value	Unit	Description
$\kappa_{p,c}$	0.6631	p.u.	proportional constant for PI current controller
$ au_{i,c}$	4	ms	time constant for PI current controller
$\kappa_{p,v}$	0.1273	p.u.	proportional constant for PI voltage controller
$ au_{i,v}$	20	ms	time constant for PI voltage controller
$k_p$	0.05	p.u.	speed droop constant
$k_q$	0.02	p.u.	voltage droop constant
$k_{pp}$	1.80	p.u.	proportional constant for dc-link protection
$ au_{pp}$	80	ms	time constant for dc-link protection
$\epsilon_1$	0.01	_	deadband constant for dc-link protection
$\epsilon_2$	0.02	_	deadband constant for dc-link protection
$ au_\omega$	50	ms	droop-control time constant
$ au_s$	5	ms	time constant for active power filter
$ au_g$	0.1	ms	time constant for grid-side current filter
$v_{mn,j}$	1.1	p.u.	minimum GSC input voltage

where: (i)  $\boldsymbol{v}_{dq}^{\rm r}$  and  $\boldsymbol{i}_{dq}^{\rm r}$  are from (24) and (84), (ii)  $\boldsymbol{v}_{dq,g}^{\rm c}$  and  $\boldsymbol{i}_{dq,g}^{\rm c}$  are from (32) and (87), illustrated in Figure 2. (iii)  $\boldsymbol{i}_{dq,L}$  and  $\boldsymbol{v}_{dq,L}$  are from (94) and (95) after using (9), respectively. The sub-vectors of  $\boldsymbol{u}$  are:

$$\boldsymbol{u}_G^\top = [V^{\star\top}, P_v^{\star\top}] \in \mathbb{R}^{2I}; \ \boldsymbol{u}_R^\top = [V^{\star\top}, P_e^{\star\top}] \in \mathbb{R}^{2J} \quad (102)$$

which are formed from (23), (17), (44) and (35).

The select outputs for assessment are:

$$\Psi_G^{\top} = [|\widetilde{\boldsymbol{V}}_{\boldsymbol{G}}|^{\top}, |\widetilde{\boldsymbol{I}}_{\boldsymbol{G}}|^{\top}, \boldsymbol{\omega}_{r}^{\top}, \boldsymbol{s}_{r}^{\top}, \boldsymbol{\delta}_{r}^{\top}]$$
 (103)

$$\Psi_R^{\top} = [|\widetilde{V}_R|^{\top}, |\widetilde{I}_R|^{\top}, \delta_c^{\top}, \omega_c^{\top}, s_c^{\top}, v_{dc}^{\top}]$$
 (104)

$$\Psi_L^{\top} = [|\widetilde{V}_L|^{\top}, |\widetilde{I}_m|^{\top}, \omega_m^{\top}, s_m^{\top}]$$
 (105)

where the magnitudes  $|\widetilde{V}_G|$  is from (83),  $|\widetilde{V}_R|$  from (86) and,  $|\widetilde{V}_L|$  from (89), (92), and (93). We use the slip of conventional plants  $s_r$ , PV stations  $s_c$ , and motors  $s_m$  where:

$$s_{\mathsf{c},j} = \frac{\omega_{\mathsf{c},j} - \omega_{\mathsf{e}}}{\omega_{\mathsf{e}}} \;, s_{\mathsf{r},i} = \frac{\omega_{\mathsf{r},i} - \omega_{\mathsf{e}}}{\omega_{\mathsf{e}}} \;, s_{m,k} = \frac{\omega_{\mathsf{e}} - \omega_{m,k}}{\omega_{\mathsf{e}}}$$
(106)

and  $\omega_e$  from (37) to ascertain synchronism from simulations.

## VI. CASE STUDIES

We demonstrate the dynamic performance of grid-forming PV power plants during transmission faults and solar irradiance disturbances. To that end, we studied modified versions of the WSCC 9-bus [28] and IEEE 39-bus power systems [55]. The system volt-ampere and speed bases are  $S_b=100$  MVA and  $\omega_b=120\pi$  rad/s. Table I and II report per-unit parameters with respect to the PV power plant rating. The specific parameters for a j-th PV plant with rating  $S_{\rm nom}^j$  in the

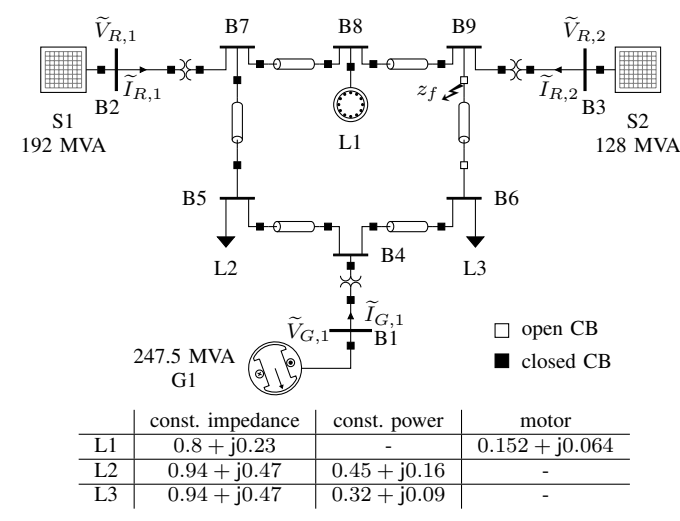


Fig. 7. One line diagram of modified WSCC power system. The impedance of the motor is given when the slip  $s_{m,1}=0.02$ .

base  $S_b$  are scaled from the values in Tables I and II as done in [36]. Additionally, we define here  $\beta^j = S_b/S_{nom}^j$  and:

$$k_{pp,j} = k_{pp}/\beta^{j}, \ \tau_{pp,j} = \tau_{pp}, \ k_{p,j} = \beta^{j}k_{p}, \ k_{q,j} = \beta^{j}k_{q}$$

$$(107)$$

$$\kappa_{p,v}^{j} = \kappa_{p,v}/\beta^{j}, \ \kappa_{p,c}^{j} = \beta^{j}\kappa_{p,c}, \ \tau_{\omega,j} = \tau_{\omega}, \ \tau_{i,v}^{j} = \tau_{i,v}$$

$$(108)$$

$$\tau_{i,c}^{j} = \tau_{i,c}, \ R_{s,j} = R_{s}\beta^{j}, \ R_{sh,j} = R_{sh}\beta^{j}, \ i_{0,j} = i_{0}/\beta^{j}.$$

$$(109)$$

The numerical studies are conducted in a desktop with 16 GB of RAM and four cores Intel® Xeon® i3 running at 3.4 GHz. The studies are implemented using MATLAB R2020a [56] and MATPOWER 7.0 [57]. The DAEs from Sections II–V are solved using the MATLAB's DAE solver ode15s. The ode15s settings are: (i)  $1\times 10^{-4}$  relative tolerance, (ii)  $1\times 10^{-3}$  absolute tolerance, and (iii)  $1\times 10^{-3}$  s maximum step size. We simulated the WSCC and IEEE systems for T=4 s and T=20.0 s, respectively. The corresponding CPU times were 5.26 s and 10.77 s.

# A. WSCC 9-Bus Grid: Fault-Ride Through Capability

The modified topology of the WSCC 9-bus grid is depicted in Fig. 7. The thermal units that existed in B2 and B3 were substituted by 192- and 128-MVA PV power plants, respectively. The load composition for this grid is specified in Fig. 7. The transient performance of the WSCC 9-bus system when impacted by a three-phase fault is illustrated in Figs. 8–10. The fault impedance  $z_f = \text{j}0.125$  p.u. and occurs close to B9 in Fig. 7. In the simulation, the fault is applied at  $t = t_f = 0.5$  s and is cleared after 5 cycles at  $t = t_c = 0.5 + 5/60$  s by opening the circuit breakers of the branch interconnecting buses B9–B6 as shown in Fig. 7.

We learn from Fig. 8 the following: (A)  $|V_{R,1}|$  (q.v. Fig. 2) can be as low as 0.57 p.u. by t=0.58 s. (B)  $|\widetilde{V}_{R,2}|$  sags to 0.37 p.u. by t=0.58 s. (C)  $|\widetilde{V}_{R,2}|$  spikes to 1.2 p.u. by t=0.61 s. (D)  $|\widetilde{I}_{R,2}|$  momentarily reaches 5.512 p.u. at t=0.50 s. (E)  $|\widetilde{I}_{R,1}|$  and  $|\widetilde{I}_{R,2}|$  drop by t=0.61 s to mitigate the voltage overshoot in (C), q.v. (26). (F)  $\omega_{\text{c,2}}$  reaches 1.015 p.u. because

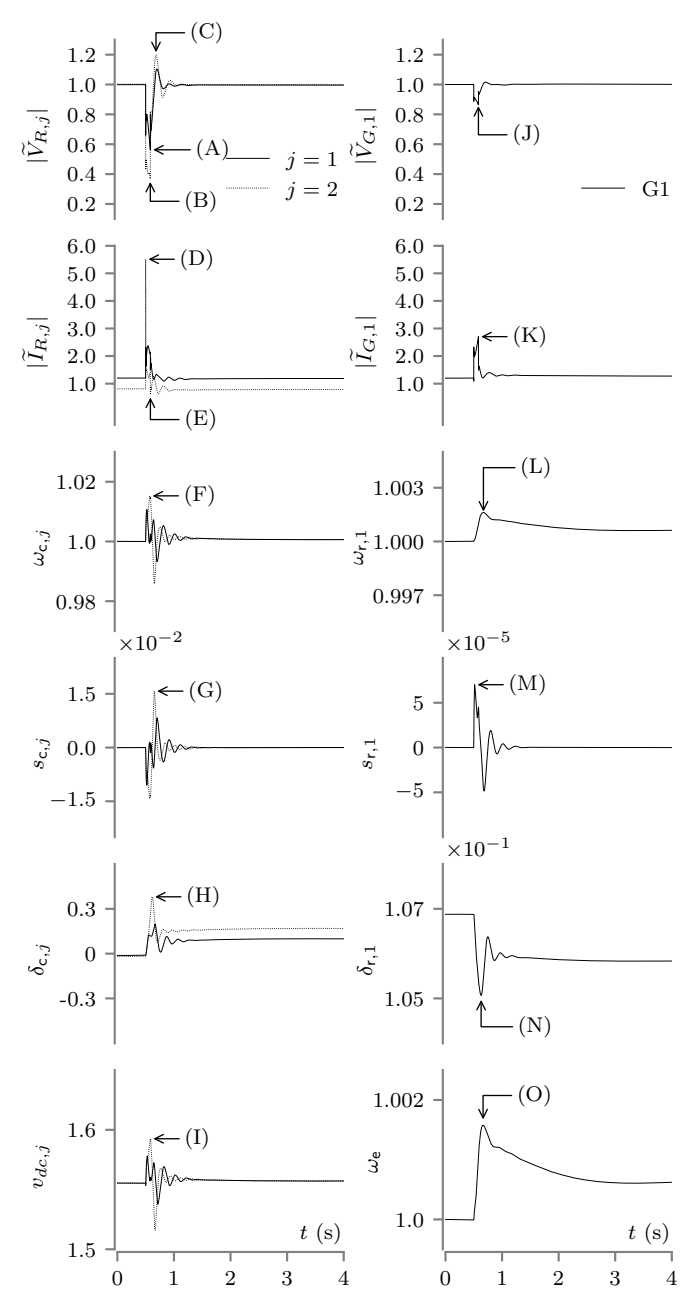


Fig. 8. WSCC 9-bus grid: Performance of PV solar and conventional power plants. Traces for S1 and S2 are with solid and dotted lines, respectively.

 $P_{e,2} \to 0$  in (34) during the fault. (G)  $s_{\text{c},2}$  deviates up to 0.015 when the fault is active as a consequence of (F). (H)  $\delta_{\text{c},1}$  and  $\delta_{\text{c},2}$  respectively increases from -0.012 to 0.186 rad and from -0.018 to 0.38 rad when the fault is active because  $\omega_{\text{c}_1}$  and  $\omega_{\text{c}_2}$  increase q.v. (36). (I) The dc-link voltage  $v_{dc,2}$  attains 1.59 p.u. during the fault because of a reduction on transferred power from the PV array to the grid q.v. (28). (J)  $|\widetilde{V}_{G,1}|$  sags to 0.86 p.u. during the fault. (K)  $|\widetilde{I}_{G,1}|$  only attains 2.7 p.u. because the fault is relatively far from G1 q.v. Fig. 7. (L)  $\omega_{\text{r},1}$  reaches 1.002 p.u. because  $T_{e,1}$  decreases in (14). (M)  $s_{r,1}$  deviation is minor because of rotor inertia. (N)  $\delta_{\text{r},1}$  decreases to 0.1058 rad from 0.1069 rad as a result of (L) and (O). (O)  $\omega_{\text{e}}$ , the speed of the center of inertia, accelerates and reaches a zenith during the fault. Notably,  $s_{\text{r},1}, s_{\text{c}1}, s_{\text{c},2} \to 0$  after the

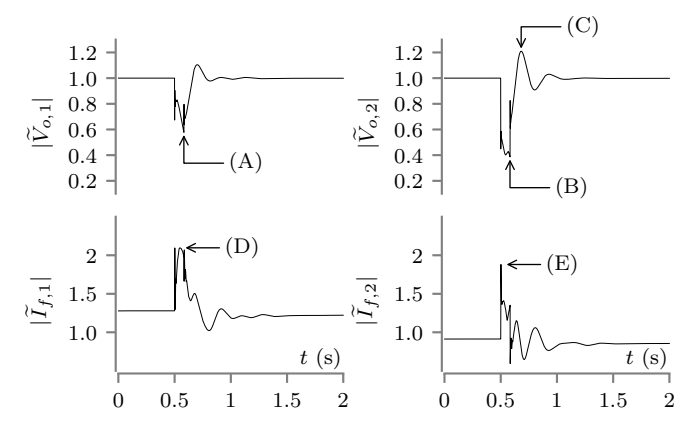


Fig. 9. WSCC 9-bus grid: Performance of PV and conventional power plants.

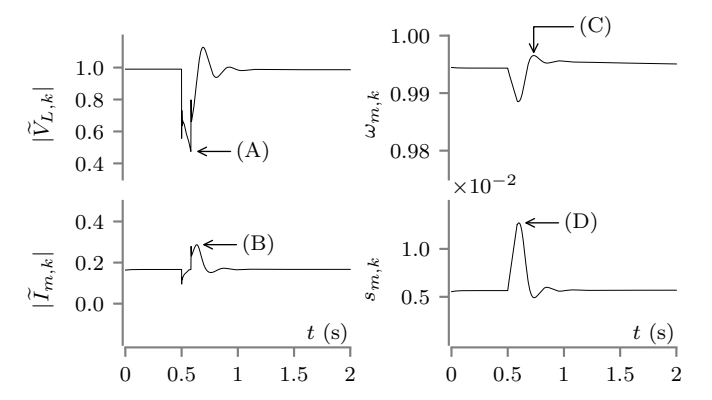


Fig. 10. WSCC 9-bus grid: Transient behavior of motor load L1 (k = 1).

fault is cleared at  $t=t_c$  s, which confirms that synchronism is maintained.

The behavior of the PV power plant variables during the fault are reported in Fig. 9 where: (A) The magnitude of  $v_{dq,o}^{c_1}$ in Fig. 2 for the PV power plant S1 drops to  $|\widetilde{V}_{o,1}| = 0.59$ p.u. by t=0.58 s. (B) Similarly, the magnitude of  $v_{dq,o}^{c_2}$ drops to  $|\widetilde{V}_{o,2}|=0.41$  p.u. by t=0.5 s. (C)  $v_{dq,o}^{\mathbf{c}_2}$  can be as high as 1.207 after the fault is cleared. (D) The current magnitude  $|\widetilde{I}_{f,1}|$  of  $i_{dq,f}^{c_1}$  in Fig. 2 rises from 1.3 to 2.095 p.u by t = 0.50 s which slightly violates the rated current  $I_{\text{mx},1} =$ 1.92 p.u. of the converter in S1. (E) The magnitude  $|I_{f,2}|$  of  $i_{dq,f}^{\mathbf{c}_2}$  reached 1.88 p.u. which violated the rating  $I_{\mathrm{mx},2}=1.28$ when the fault was applied. Nonetheless, this short-lived current magnitude lasted less than 15 ms because  $|I_{f,2}|$  was immediately steered towards the rated current  $I_{mx,2} = 1.28$ p.u. by the grid-forming regulator in Section III-D. The impact of this trespassing on GSC semiconductor temperature might be minor. We recall from Fig. 3a that the radius to saturate dq-current commands in S2, for example, is  $I_{mx,2} = 1.28$  p.u.

We report the response of the motor L1 in Fig. 7 for  $H_{m,1}=0.5$  s for (90) and  $K_{m,1}=0.15$  for (91). In Fig. 10, we learn that: (A)  $|\widetilde{V}_{L,1}|$  sags to 0.573 p.u. by t=0.58 s. (B)  $|\widetilde{I}_{m,1}|$  increases to 0.286 p.u. because motor slip in (89) increases. (C)  $\omega_{m,1}$  reaches 0.9895 p.u. because  $\omega_{\rm e}$  accelerates. (D)  $s_{m,1}$  reaches 0.011 during the fault; in steady state,  $s_{m,1}=0.005$ .

We note here that the PV power plants of Fig. 7 must remain

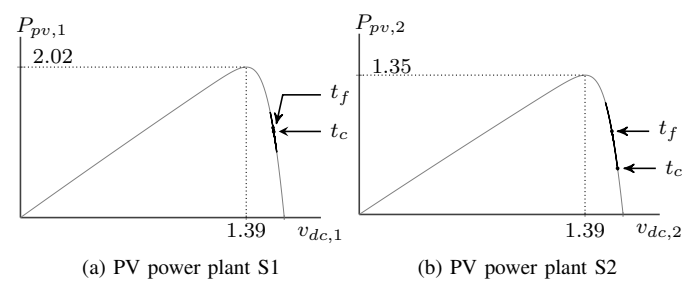


Fig. 11. Power and voltage characteristics (gray) of the PV arrays in Fig. 7. The loci for power plants S1 and S2 during the fault are the solid-black traces. The fault is applied at  $t_f = 0.5$  s and cleared at  $t_c = 0.5 + 5/60$  s.

connected during the fault to comply with the North American Electric Reliability Corporation (NERC) standard PRC-024-3 [32] because: (i)  $|V_{R,1}|, |V_{R,2}| \in [0, 1.2]$  during the fault event in Fig. 8. According to the voltage duration envelope in [32, p. 18], power plants are allowed to trip, for example, if  $|V_{R,j}| \notin [0.0, 1.2]$  for more than 150 ms. (ii)  $\omega_{c,1}, \omega_{c,2} \in$ [0.96, 1.03] for less than 30 s [32, p. 18]. Power plants are allowed to trip, for example, if  $\omega_{c,1}$ ,  $\omega_{c,2} \notin [0.96, 1.03]$  for more than 30 s [32, p. 17]. We emphasize that although there was a short-lived violation of  $I_{mx,2}$  (for less than 15 ms), the PV power plant S2 is not allowed to trip to comply with [32, p. 17]. Hence, a hypothetical operator of the IEEE 9-bus power system could have used these simulation results to contrast them against the technical specifications of PV power plants to ascertain compliance with grid standards and determine corrective actions if deemed necessary. Similar studies can be conducted to test compliance with recent standards, e.g., the standard IEEE P2800 [33].

The responses of the S1 and S2 PV arrays in Fig. 7 during the fault are reported in Fig. 11. We learn from this figure that  $v_{dc,2}$  at  $t=t_c=0.5+5/60\,\mathrm{s}$  is greater than  $v_{dc,2}$  at  $t=t_f=0.5\,\mathrm{s}$  because the power injected by S2 reduces as the fault is relatively close, q.v. Fig. 7. The impact of the fault on  $v_{dc,1}$  is minor because the fault is relatively far from S1. We also note in Fig. 11 that during the fault,  $v_{dc,j}>v_{dc,j}^*=1.39\,\mathrm{p.u.}$  for j=1,2; hence, the active dc-link protection of Section IV-B does not operate. Nonetheless, the protection can activate when solar irradiance drops and the GSC injects more ac power than can be supplied by the PV array, q.v. Section IV-B.

## B. WSCC 9-Bus Grid: Dc-Link Voltage Protection

We demonstrate the functionality of the active dc-link protection in Section IV-B. The parameters of the voltage and current regulators are the same ones that were used in Section VI-A. We show that variations of solar irradiance can lead to loss of synchronism of grid-forming PV power plants. To that end, we study the performance of S2 in Fig. 7 during a step drop in solar irradiance:

$$I_{r,2}(t) = \begin{cases} 1000 \text{ W/m}^2 & t \in [0, 2.5) \cup [5.0, 7.5] \text{ s} \\ 400 \text{ W/m}^2 & t \in [2.5, 5.0) \text{ s} . \end{cases}$$
(110)

The solar irradiance at S1 is  $I_{r,1}(t)=1000~{\rm W/m^2}$  for  $t\in[0,7.5]$  s. In Fig. 12, we report the results of two simulation instances: with and without the active protection.

When the protection is absent, we learn from Fig. 12: (A)  $v_{dc,2}$  falls to 0.62 p.u. (B)  $P_{cv,2}$  falls to -1.25 p.u. (C)  $P_{pv,2}$  sags to -1.16 p.u. (D) slip  $s_{\rm c,2}$  drops to -0.09. All this because low values of  $v_{dc,2}$  impacts (51) by t=3.1 s, hence S2 loses synchronism and the simulation terminates.

When the protection is active, we observe in Fig. 12: (E)  $v_{dc,2}$  drops only to 1.26 p.u., hence, synchronism is not lost. We note that  $v_{dc,2}$  settles around 1.32 p.u after t=2.5 s. (F)–(G) The estimated variable  $i_{g,2}$  follows the changes of  $i_{g,2}$ . We recall that  $i_{g,2}$  is used to calculate  $E_{dc,2}^*([2.5,5.0]) = 1.87$ p.u. (which implies  $\hat{v}_{dc,2}^*([2.5,5.0]) = 1.37$ ), q.v. Section IV. The value of  $E_{dc,2}^*$  is the set-point to steer  $\Delta P_{e,2}^*$  to modulate  $P_{cv,2}$  for MPP tracking as explained in Section IV-B. (H)  $\Delta P_{e,2}^{\star}$  attains 0.78 p.u. by t = 2.63 s. This to reduce the converter ac power  $P_{cv,2}$ , q.v., (28) and (29). After t > 5s,  $\Delta P_{e,2}^{\star}$  resets because irradiance rises. The two notches of  $\Delta P_{e,2}^{\star}$  by  $t=2.5~\mathrm{s}$  and  $t=5.0~\mathrm{s}$  in Fig. 12 appear because the set point  $\widehat{E}_{dc,2}^*$  for (79)–(82) changes abruptly as a result of the two step-wise changes in solar irradiance in (110). We recall that  $E_{dc,2}^*$  is estimated in Section IV-A. (I)  $P_{cv,2}$  oscillates while approaching the MPP because of the concave behavior of the PV array, q.v. Section III-E as well as the piece-wise response of the dc-link protection, q.v. Section IV-B. The frequency of these control-induced oscillations is 5 Hz ca. (J)  $P_{pv,2}$  momentarily drops from 0.8 to 0.14 p.u. and recovers to 0.5 p.u. (K)  $s_{c,2}$  deviates up to only 0.004 which confirms that synchronization problems do not exist. (L) The voltage  $|V_{o,2}|$  oscillates between [0.998, 1.001] p.u by t = 2.6 s and decays to 0.9997 p.u. by t = 5 s. (M)  $|I_{f,2}|$  oscillates between [0.46, 0.75] p.u by t = 2.6 s and decays to 0.64 p.u. by t=5 s. These short-lived oscillations are not detrimental to the PV power plant because they do not impact mechanical components. All the aforementioned observations suggest that the proposed dc-link protection performs well.

# C. IEEE 39-Bus Grid: Fault-Ride Through Capability

We modified the system in [55] by substituting the 1000-MVA generators connected to buses B34 and B36 with two PV power plants S5 and S7 of the same rating, respectively. We studied the response of the system to a five-cycle fault near bus eight B8 in [55, Fig. 1]. The fault was applied at t=0.50 s and removed at t=0.5+5/60 s. This did not cause stability problems as evidenced in Fig. 13. In particular, voltage magnitudes and speed values of the PV plants and conventional ones converged close to nominal after the fault was cleared. If the fault had remained active for more than seven cycles, the synchronous machines G2 connected to bus B31 and G3 connected to bus B32 would have lost synchronism.

From Fig. 13, we infer the following: (A) The voltage magnitude,  $|\widetilde{V}_{R,7}|$  at the terminal of PV power plant S7 sags to 0.85 p.u. at t=0.50 s. (B) The current magnitude,  $|\widetilde{I}_{R,5}|$  spikes to 9.63 p.u. at t=0.50 s from 6.806 p.u. (C) The current magnitude  $|\widetilde{I}_{R,7}|$  reaches 7.98 p.u. at t=0.50 s. (D) The speed  $\omega_{\text{c,7}}$  reaches 1.004 p.u. during the fault. (E) The slip  $s_{\text{c,7}}$  deviates up to 0.004 at t=0.60 s as a consequence of (D). (F)–(G) The angles  $\delta_{\text{c,5}}$  and  $\delta_{\text{c,7}}$  respectively increase from -0.38 to -0.26 rad and from -0.33 to -0.198 rad when

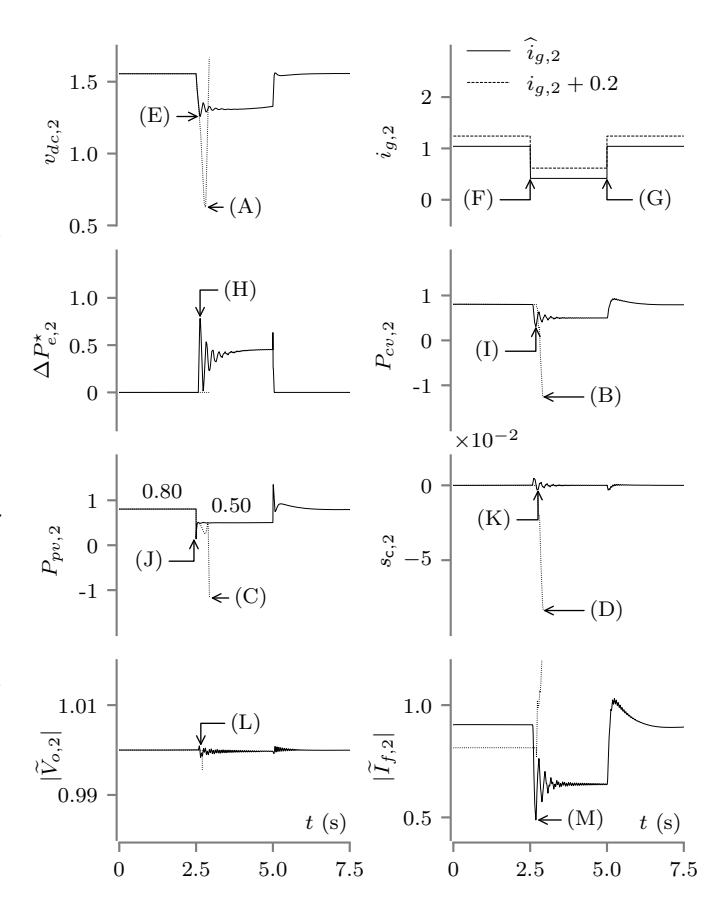
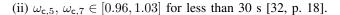


Fig. 12. WSCC 9-bus grid: Performance of renewable plant S2 during solar irradiance drop without (dotted line) and with (solid line) dc-link protection.

the fault is active because  $\omega_{c_5}$  and  $\omega_{c_7}$  increase q.v. (36). (H) The dc-link voltage  $v_{dc,5}$  slightly rises to 1.575 p.u during the fault. (I) The voltage magnitude,  $|\widetilde{V}_{G,3}|$  of the machine connected to bus 32 sags to 0.68 p.u. at t=0.58 s. (J) The current magnitude,  $|\widetilde{I}_{G,1}|$ , spikes to 18.92 p.u. at t=0.51 s because G1 is relatively close to the fault occurring in bus B8. (K) The speed  $\omega_{r,2}$  reaches 1.007 p.u. at t=0.593 s because G2 is also close to the fault. (L) The slip  $s_{r,2}$  deviates up to 0.006 at t=0.59 s which is indicative that G2 has the potential to lose synchronism. (M) The angle  $\delta_{r,2}$  increases to 1.505 rad at t=1.07 s which is the largest because of (L). (N) The synchronous speed  $\omega_{\rm e}$  reaches 1.002 p.u. at t=1.7 s and later converges to the rated value which is indicative that there are no frequency problems.

The behavior of the PV power plants during the fault are reported in Fig. 14 where: (A) The magnitude of  $v_{dq,o}^{c_5}$  in Fig. 2 for PV power plant S5 drops to  $|\widetilde{V}_{o,5}| = 0.88$  p.u. by t = 0.5 s. (B) Similarly, the magnitude of  $v_{dq,o}^{c_7}$  drops to  $|\widetilde{V}_{o,7}| = 0.88$  p.u. by t = 0.5 s. (C)  $|\widetilde{V}_{o,5}|$  can be as high as 1.13 after the fault is cleared. (D) The current magnitude  $|\widetilde{I}_{f,5}|$  rises from 5.5 to 7.94 p.u by t = 0.50 s, the rated current of S5  $I_{\text{mx},5} = 10$  p.u. (E) The magnitude  $|\widetilde{I}_{f,7}|$  reached 7.5 p.u. when the fault was applied; here,  $I_{\text{mx},7} = 10$  p.u. The PV power plants of this case study must also remain connected to comply with NERC standard PRC-024-3 [32] because: (i)  $|\widetilde{V}_{R,5}|$ ,  $|\widetilde{V}_{R,7}| \in [0,1.2]$  during the fault event in Fig. 13 and



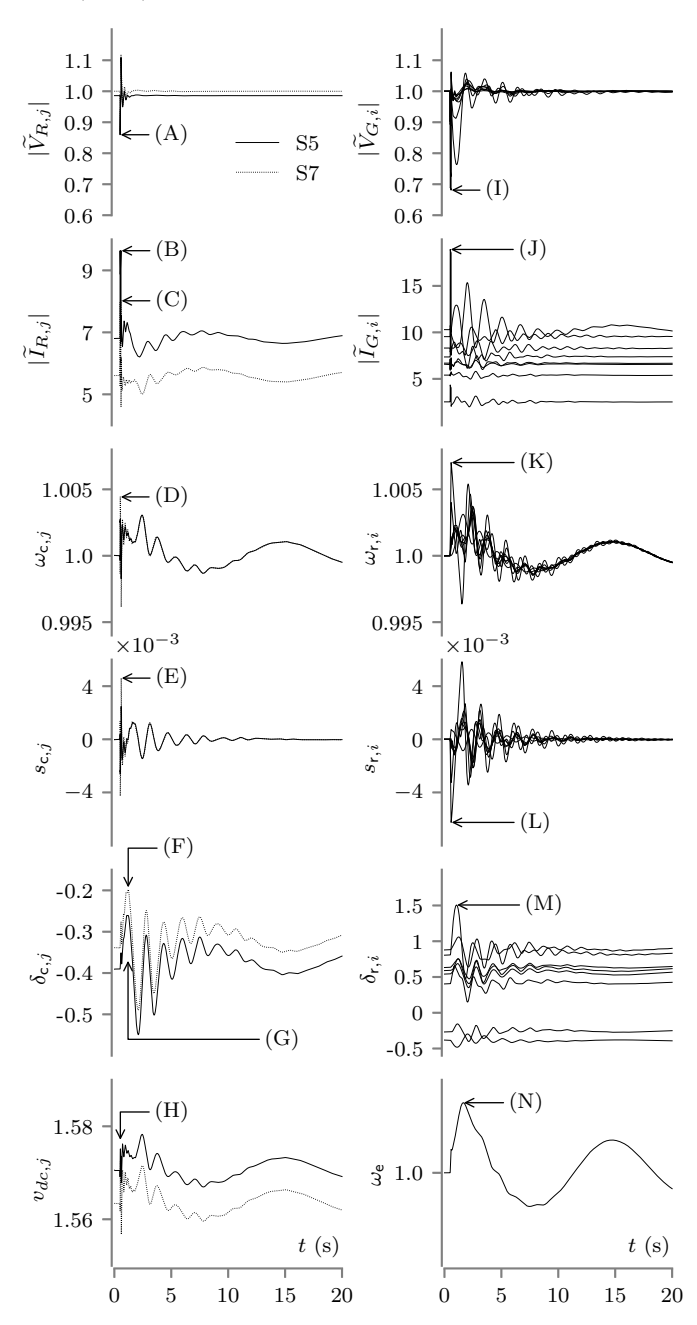


Fig. 13. IEEE 39-bus grid: Performance of PV solar and conventional power plants. Traces for S5 and S7 are with solid and dotted lines, respectively.

# VII. CONCLUSION

This paper has reported a positive-sequence model of a grid-forming PV solar power plant with fault ride-through capability and dc-link voltage protection. To this end, we engineered two-axis anti-windup PI regulators to limit dq voltage and current commands within a circle. Further, we demonstrated via simulation that grid-forming plants can lose synchronism when solar irradiance drops. This problem was mitigated by engineering an active dc-link protection scheme. The models were purposely leveraged in positive-sequence domain to mitigate the computational burden of EMT studies [58]. In general, the contributions of this paper are significant to study

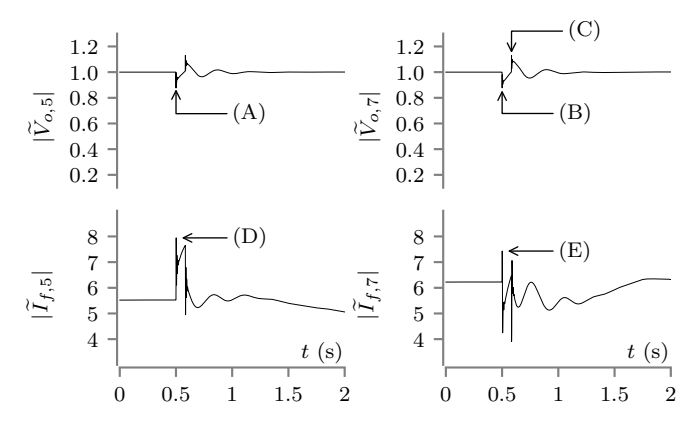


Fig. 14. IEEE 39-bus grid: Performance of PV solar and conventional power plants.

the dynamic performance of bulk power systems with ultrahigh penetrations of grid-forming PV assets during faults and solar disturbances. Notably, a power system analyst can use the advances in this paper to ascertain compliance of grid-forming PV power plants with interconnection standards [32], [33]. Also, this work can be instrumental to quantify the impact of conventional power plants on the dynamics of PV assets using, for example, linearization techniques, albeit this was not done in this paper.

An important research direction is to model PV-array blocking diodes to study the impacts of full solar irradiance outages, e.g., using PLECS [59]. Further, it is of interest to investigate the interaction of sub-transient dynamics of synchronous machinery with grid-forming assets as well as the impact of the variation of grid-forming control parameters, e.g.,  $\tau_{s,j}$  in (30). An additional research avenue consists of ascertaining the set of all possible current magnitudes at the inverter terminals of grid-forming PV power plants, e.g., using reachability analysis [60], [61]. Finally, future research will extend this framework to grid-forming power plants powered by wind and battery energy resources.

# VIII. ACKNOWLEDGEMENT

We thank the anonymous Reviewers for their assertive comments which helped improve this paper.

#### REFERENCES

- Q. Fu, A. Nasiri, V. Bhavaraju, A. Solanki, T. Abdallah, and C. Y. David, "Transition management of microgrids with high penetration of renewable energy," *IEEE Trans. Smart Grid*, vol. 5, no. 2, pp. 539–549, Nov. 2013.
- [2] E. Alegria, T. Brown, E. Minear, and R. H. Lasseter, "CERTS microgrid demonstration with large-scale energy storage and renewable generation," *IEEE Trans. Smart Grid*, vol. 5, no. 2, pp. 937–943, Nov. 2013.
- [3] Y. Lin et al., "Research roadmap on grid-forming inverters," National Renewable Energy Lab. (NREL), Golden, CO, USA, Tech. Rep. NREL/TP-5D00-73476, 2020.
- [4] "Solar futures study," U.S Department of Energy, Office of Energy Efficiency & Renewable Energy, Washington DC, USA, Tech. Rep., Sep. 2021.
- [5] B. Kroposki et al., "Achieving a 100% renewable grid: operating electric power systems with extremely high levels of variable renewable energy," *IEEE Power Energy Mag.*, vol. 15, no. 2, pp. 61–73, 2017.
- [6] V. Purba, B. B. Johnson, S. Jafarpour, F. Bullo, and S. V. Dhople, "Dynamic aggregation of grid-tied three-phase inverters," *IEEE Trans. Power Syst.*, vol. 35, no. 2, pp. 1520–1530, Sep. 2019.

- [7] P. Unruh, M. Nuschke, P. Strauß, and F. Welck, "Overview on grid-forming inverter control methods," *Energies*, vol. 13, no. 10, p. 2589, May 2020.
- [8] M. C. Chandorkar, D. M. Divan, and R. Adapa, "Control of parallel connected inverters in standalone ac supply systems," *IEEE Trans. Ind. Appl.*, vol. 29, pp. 136–143, Feb. 1993.
- [9] M. N. Marwali, J.-W. Jung, and A. Keyhani, "Control of distributed generation systems-part II: Load sharing control," *IEEE Trans. Power Electron.*, vol. 19, no. 6, pp. 1551–1561, Nov. 2004.
- [10] N. Pogaku, M. Prodanovic, and T. C. Green, "Modeling, analysis and testing of autonomous operation of an inverter-based microgrid," *IEEE Trans. Power Electron.*, vol. 22, no. 2, pp. 613–625, Mar. 2007.
- [11] P. Piagi and R. H. Lasseter, "Autonomous control of microgrids," in 2006 IEEE Power Eng. Soc. General Meeting, Montreal, Canada, Jun. 2006, pp. 8–16.
- [12] J. M. Guerrero, M. Chandorkar, T.-L. Lee, and P. C. Loh, "Advanced control architectures for intelligent microgrids—part I: Decentralized and hierarchical control," *IEEE Trans. Ind. Electron.*, vol. 60, no. 4, pp. 1254–1262, Apr. 2012.
- [13] B. B. Johnson, S. V. Dhople, A. O. Hamadeh, and P. T. Krein, "Synchronization of parallel single-phase inverters with virtual oscillator control," *IEEE Trans. Power Electron.*, vol. 29, no. 11, pp. 6124–6138, Nov. 2013.
- [14] U. Tamrakar, D. Shrestha, M. Maharjan, B. P. Bhattarai, T. M. Hansen, and R. Tonkoski, "Virtual inertia: Current trends and future directions," *Appl. Sciences*, vol. 7, no. 7, p. 654, Jun. 2017.
- [15] W. Du, Z. Chen, K. P. Schneider, R. H. Lasseter, S. P. Nandanoori, F. K. Tuffner, and S. Kundu, "A comparative study of two widely used grid-forming droop controls on microgrid small-signal stability," *IEEE Trans. Emerg. Sel. Topics Power Electron.*, vol. 8, no. 2, pp. 963–975, 2019.
- [16] Y. Li, Y. Gu, Y. Zhu, A. Junyent-Ferré, X. Xiang, and T. C. Green, "Impedance circuit model of grid-forming inverter: Visualizing control algorithms as circuit elements," *IEEE Trans. Power Electron.*, vol. 36, no. 3, pp. 3377–3395, 2020.
- [17] R. Rosso, X. Wang, M. Liserre, X. Lu, and S. Engelken, "Grid-forming converters: Control approaches, grid-synchronization, and future trendsa review," *IEEE Open J. Ind. Appl.*, Apr. 2021.
- [18] K. S. Ratnam, K. Palanisamy, and G. Yang, "Future low-inertia power systems: Requirements, issues, and solutions-a review," *Renew. Sustain. Energy Rev.*, vol. 124, p. 109773, May 2020.
- [19] B. J. Pierre et al., "Bulk power system dynamics with varying levels of synchronous generators and grid-forming power inverters," in 46th Photovolt. Specialists Conf., Chicago, IL, USA, Jun. 16-21 2019, pp. 0880–0886.
- [20] NERC, "Odessa disturbance," North American Electric Reliability Corporation, Atlanta, GA, USA, Tech. Rep., Sep. 2021.
- [21] NERC & WECC staff report, "San Fernando Disturbance," North American Electric Reliability Corporation, Atlanta, GA, USA, Tech. Rep., Nov. 2020.
- [22] —, "April and may 2018 fault induced solar photovoltaic resource interruption disturbances report: southern california events: April 20, 2018 and may 11, 2018," North American Electric Reliability Corporation, Atlanta, GA, USA, Tech. Rep., May 2018.
- [23] —, "900 MW fault induced solar photovoltaic resource interruption disturbance report," North American Electric Reliability Corporation, Atlanta, GA, USA, Tech. Rep., Feb. 2018.
- [24] —, "1,200 MW fault induced solar photovoltaic resource interruption disturbance report," North American Electric Reliability Corporation, Atlanta, GA, USA, Tech. Rep., Jun. 2017.
- [25] N. M. Haegel et al., "Terawatt-scale photovoltaics: Transform global energy," Sci., vol. 364, no. 6443, pp. 836–838, May 2019.
- [26] M. Al-Muhaini and G. T. Heydt, "Evaluating future power distribution system reliability including distributed generation," *IEEE Trans. Power Del.*, vol. 28, no. 4, pp. 2264–2272, 2013.
- [27] R. Rüdenberg, Transient performance of electric power systems: phenomena in lumped networks. MIT press, 1969.
- [28] V. Vittal and J. D. McCalley, Power system control and stability, 3rd ed. Hoboken, NJ, USA: Wiley, 2019.
- [29] P. W. Sauer, M. A. Pai, and J. H. Chow, Power System Dynamics and Stability: With Synchrophasor Measurement and Power System Toolbox. Hoboken, NJ, USA: Wiley, 2017.
- [30] O. Wasynczuk, S. D. Sudhoff, T. D. Tran, D. Clayton, and H. Hegner, "A voltage control strategy for current-regulated PWM inverters," *IEEE Trans. Power Electron.*, vol. 11, no. 1, pp. 7–15, Jan. 1996.

- [31] K. Aström and T. Hagglünd, PID controllers, theory, design, and tunning, 2nd ed. Research Triangle Park, NC: Instrument Society of America, 1994.
- [32] Frequency and Voltage Protection Settings for Generating Resources, NERC Reliability Standard PRC-024-3, Jul 2020.
- [33] IEEE Draft Standard for Interconnection and Interoperability of Inverter-Based Resources (IBR) Interconnecting with Associated Transmission Electric Power Systems, IEEE Std. P2800/D6.3, Mar 2021.
- [34] A. Yazdani and R. Iravani, Voltage-Sourced Converters in Power Systems. Hoboken, NJ, USA: Wiley, 2010.
- [35] V. Purba, S. V. Dhople, S. Jafarpour, F. Bullo, and B. B. Johnson, "Reduced-order structure-preserving model for parallel-connected threephase grid-tied inverters," in *Proc. 18th Workshop Control and Model. Power Electron.*, Stanford, CA, USA, Jul. 9-11 2017, pp. 1–7.
- [36] H. N. Villegas Pico and B. B. Johnson, "Transient stability assessment of multi-machine multi-converter power systems," *IEEE Trans. Power Syst.*, vol. 34, no. 5, pp. 3504–3514, Sept. 2019.
- [37] A. Fernández-Guillamón, A. Vigueras-Rodríguez, and Á. Molina-García, "Analysis of power system inertia estimation in high wind power plant integration scenarios," *IET Renew. Power Gener.*, vol. 13, no. 15, pp. 2807–2816, 2019.
- [38] R. Lasseter and P. Piagi, "Providing premium power through distributed resources," in *Proc. 33rd Hawaii Int. Conf. Syst. Sciences*, Maui, HI, USA, Jan. 7 2000, pp. 1–9.
- [39] J. Liu, Y. Miura, and T. Ise, "Comparison of dynamic characteristics between virtual synchronous generator and droop control in inverterbased distributed generators," *IEEE Trans. Power Electron.*, vol. 31, no. 5, pp. 3600–3611, 2015.
- [40] J. Alipoor, Y. Miura, and T. Ise, "Power system stabilization using virtual synchronous generator with alternating moment of inertia," *IEEE Trans. Emerg. Sel. Topics Power Electron.*, vol. 3, no. 2, pp. 451–458, 2014.
- [41] T. Shintai, Y. Miura, and T. Ise, "Oscillation damping of a distributed generator using a virtual synchronous generator," *IEEE Trans. Power Del.*, vol. 29, no. 2, pp. 668–676, 2014.
- [42] A. Ademola-Idowu and B. Zhang, "Frequency stability using MPC-based inverter power control in low-inertia power systems," *IEEE Trans. Power Syst.*, vol. 36, no. 2, pp. 1628–1637, 2020.
- [43] P. C. Krause, O. Wasynczuk, S. D. Sudhoff, and S. D. Pekarek, Analysis of Electric Machinery and Drive Systems, 3rd ed. John Wiley & Sons, 2013
- [44] M. G. Villalva, J. R. Gazoli, and E. R. Filho, "Comprehensive approach to modeling and simulation of photovoltaic arrays," *IEEE Trans. Power Electron.*, vol. 24, no. 5, pp. 1198–1208, Mar. 2009.
- [45] S. P. Boyd and L. Vandenberghe, Convex Optimization. Cambridge university press, 2004.
- [46] J. Nachbar, "Concave and convex functions," 2018, accessed: 2021-09-14. [Online]. Available: https://sites.wustl.edu/nachbar/coursenotes/math/convexity/
- [47] H. K. Khalil, Nonlinear Systems, 3rd ed. Upper Saddle River, NJ: Prentice Hall, 2002.
- [48] D. R. Kincaid and E. W. Cheney, Numerical Analysis: Mathematics of Scientific Computing. Amer. Math. Soc., 2009, vol. 2.
- [49] SUNNY CENTRAL 2200 / 2475 / 2500-EV / 2750-EV / 3000-EV, SMA Solar Technology. [Online]. Available: https://files.sma.de/downloads/SC2200-3000-EV-DS-en-59.pdf
- [50] N. Wang and H. Adeli, "Algorithms for chattering reduction in system control," *Journal of Franklin Inst.*, vol. 349, no. 8, pp. 2687–2703, Oct. 2012.
- [51] A. M. Annaswamy, F. P. Skantze, and A.-P. Loh, "Adaptive control of continuous time systems with convex/concave parametrization," *Automatica*, vol. 34, no. 1, pp. 33–49, Jan. 1998.
- [52] J. V. Milanović and I. A. Hiskens, "Effects of dynamic load model parameters on damping of oscillations in power systems," *Electric Power Syst. Res.*, vol. 33, no. 1, pp. 53–61, Apr. 1995.
- [53] —, "Load modelling in studies of power system damping," *IEEE Trans. Power Syst.*, vol. 10, no. 4, pp. 1781–1788, Nov. 1995.
- [54] NERC, "Dynamic load modeling," North American Electric Reliability Corporation, Atlanta, GA, USA, Tech. Rep., Dec. 2016.
- [55] I. Hiskens, "IEEE PES task force on benchmark systems for stability controls," IEEE PES, Piscataway, NJ, USA, Tech. Rep., Nov. 2013.
- [56] MATLAB, version 9.8.0 (R2020a). Natick, Massachusetts: The Math-Works Inc., 2020.
- [57] R. D. Zimmerman, C. E. Murillo-Sanchez, and R. J. Thomas, "MAT-POWER: Steady-state operations, planning and analysis tools for power systems research and education," *IEEE Trans. Power Syst.*, vol. 26, no. 1, pp. 12–19, Feb. 2011.

- [58] S. Subedi et al., "Review of methods to accelerate electromagnetic transient simulation of power systems," IEEE Access, vol. 3, Jun. 2021.
- [59] Plexim Inc., PLECS: The simulation platform for power electronic systems, v4.5 ed., (2021). Accessed: Nov. 17, 2021. [Online]. Available: https://plexim.com/download/documentation.
- [60] H. N. Villegas Pico and D. C. Aliprantis, "Voltage ride-through capability verification of wind turbines with fully-rated converters using reachability analysis," *IEEE Trans. Energy Convers.*, vol. 29, no. 2, pp. 392–405, 2014.
- [61] H. N. Villegas Pico, D. C. Aliprantis, and X. Lin, "Transient stability assessment of power systems with uncertain renewable generation," in Proc. 10th Bulk Power Syst. Dyn. Control Symp., 2017, pp. 1–13.



Soummya Roy (S'21) received his B.Tech degree in electrical and electronics engineering from the National Institute of Technology, Warangal, India, 2016 and his M.S degree in electrical engineering from Iowa State University, Ames, IA, USA in 2020. Soummya is currently pursuing the Ph.D. degree in electrical engineering at Iowa State University, Ames, IA, USA. His research interests are in the intersection of power system modeling, dynamics and control.



At present, Hugo is a Harpole-Pentair Assistant Professor in the Department of Electrical and Computer Engineering at Iowa State University. Hugo was a Post-Doctoral Researcher of Power Engineering at the National Renewable Energy Laboratory, Golden, CO, USA for 2017–2019 and a Post-Doctoral Research Assistant at Purdue University, West Lafayette, IN, USA for 2016–2017. Hugo was a Supervisor of electrical maintenance in CELEC EP Termipichincha, Ecuador, for 2007–2009, where he led several projects on control, automation, and protection of power plants with diesel generator sets.

Hugo's research interests lie at the intersection of renewable energy conversion, power system dynamics, power restoration processes, control systems, and computational analysis of dynamical systems.